MINISTÈRE DE
L'ENSEIGNEMENT SUPÉRIEUR
ET DE LA RECHERCHE
SCIENTIFIQUE

Université
Félix Houphouët Boigny

UNITÉ DE FORMATION ET DE
RECHERCHE-SCIENCES DES
STRUCTURES DE LA
MATIÉRE ET DE
TECHNOLOGIE

REPUBLIQUE DE CÔTE D'IVOIRE
UNION-DISCIPLINE-TRAVAIL

839

MASTER IN ENERGY AND GREEN HYDROGEN

SPECIALITY: Green Hydrogen Production and Technology

MASTER THESIS:

Subject/Topic:

DEVELOPMENT OF ACCESSIBLE AUTOMATED QUANTIFICATION METHODS ON FIB/SEM TOMOGRAPHY FOR INVESTIGATING SOLID OXIDE ELECTROLYZER CELL (SOEC) AND PROTON EXCHANGE MEMBRANE WATER ELECTROLYZER (PEMWE) DEGRADATION

Presented the 26th September and by:

Adolé Imelda Akue-Goeh

Jury

Dr(MC) ZORO Emma Georgina	**President**
Prof. ESSI Marc Marie-Maurice Mélèdge	**Examiner**
Dr. FOFANA Daouda	**Supervisor**
Prof. Dr. Rüdiger-A.Eichel	**Co-Supervisors**
Dr. Junbeom Park	

Academic year: 2024-2025

FOREWORD AND ACKNOWLEDGEMENTS

I would like to acknowledge and express my sincere gratitude to the following individuals and organizations who have played an important role in shaping my educational journey and academic success.

I am truly grateful BMFTR and WASCAL for awarding me this scholarship that has made my educational journey possible. Their support has been invaluable in helping me pursue my goals.

I extend my thanks to the president of the University Félix Houphouët Boigny, Prof. Ballo Zieto, the president of the University Abdoul Moumouni, Prof. Moussa Baragé, and to the president of the University of Lomé, Prof. Adama Mawulé Kpodar Saidou. I am grateful to the vice chancellor of Forschungszentrum Jülich and the director of the institute IET-1, where I completed my internship. My thanks to the team members from Côte d'Ivoire, Togo, and Niger, who were involved in the first, second and third semesters of my academic journey, for their collaboration and support.

I am sincerely grateful to my Co-Supervisor, Prof. Dr. Rüdiger-A. Eichel for his consistent support and expert guidance throughout my academic journey.

I extend my thanks to my Major-Supervisor, Dr. FOFANA Daouda, for his valuable insights and contributions that have enhanced the quality of my academic work. I would like to acknowledge the jury president, Dr (MC) ZORO Emma Georgina and the jury examiner Prof. ESSY Marc Marie-Maurice Mélèdge for their precious time and expertise in assessing my academic work.

I am particularly grateful to my parents, Adovi Akue-Goeh N'Bueke and my mother, Mensanvi Kokoe Chantal-Clarisse as well as my brothers Jovani and Eloïse Akue-Goeh, who have been nothing but supportive and caring throughout my life. I feel very lucky to be surrounded by such a loving family. My thanks also my friends for their continual constructive insight.

My sincere gratitude goes to Dr. Shibabrata Basak the head of in-situ Electron Microscopy, for his expert leadership and support. I cannot end these acknowledgments without mentioning my daily supervisor, Dr. Junbeom Park, for his unwavering support, insightful advice and constant availability throughout this internship. His guidance was invaluable in overcoming challenges and advancing my research. I sincerely appreciate the positive environment that both have created during my stay. A special thanks are also extended to all members of the IET-1 team.

ABSTRACT

The expanding hydrogen economy relies on efficient and durable electrochemical devices, such as Solid Oxide Electrolysis Cells (SOECs) and Proton Exchange Membrane Water Electrolyzers (PEMWEs). The performance and lifetime of these devices are closely linked to their microstructural properties. Despite the development of advanced microstructural characterization techniques, like Focused Ion Beam-Scanning Electron Microscopy (FIB-SEM) for quantitative analysis, data processing remains challenging due to the complexity of the data, the large volume generated and the limited access to advanced computational tools.

This study proposes an automated, modular pipeline that combines traditional image processing and Random Forest-based supervised learning to segment the electrode-catalyst part composed of four layers in SOECs (Layer 1 to Layer 4) and to quantitatively evaluate key microstructural parameters such as porosity and thickness. The pipeline is intentionally designed to require minimal computational resources and remain accessible even to non-expert users.

The training on a representative annotated dataset of FIB-SEM images (10 training images out of a total of 200) achieved a layer segmentation accuracy of 68% on the test dataset. Even though this indicates the need for additional improvement, it was enough to identify meaningful structural variations. The utilization of the pipeline across multiple experimental FIB-SEM datasets enables the extraction of statistically consistent trends in porosity and thickness under different operational conditions: pristine, 100-hour and 200-hour run cells. layer 4 exhibits a distinct rise in porosity, whereas layer 2 displayed a noticeable change in thickness.

These findings show that a lightweight machine learning approach combined with traditional image processing can provide meaningful insights into microstructural parameters. it also emphasizes the potential for developing a user-friendly and automated pipeline to assess the complex FIB-SEM datasets of these electrochemical devices quantitatively in a record time. Potential enhancement could look closer to the annotation protocol, feature engineering and combined machine learning approaches.

Keywords: FIB-SEM, microstructural analysis, Random Forest, image processing, electrolysis.

RESUME

La croissance de l'économie hydrogène repose sur le bon fonctionnement et la durabilité de dispositifs électrochimiques, tels que les cellules d'électrolyse à oxyde solide (SOEC) et les électrolyseurs à membrane échangeuse de protons (PEMWE). Leur performance et leur durée de vie sont en grande partie fonction de leurs propriétés microstructurelles. Malgré l'évolution des techniques avancées de caractérisation microstructurale telle que la microscopie électronique à balayage à faisceau d'ions focalisés (FIB-SEM) pour l'analyse quantitative, le traitement des données reste difficile en raison de leur complexité, du volume important d'images généré et de l'accès restreint aux outils informatiques avancés.

Cette étude présente un pipeline automatisé et modulaire qui combine les méthodes classiques de traitement d'image et l'apprentissage supervisé basé sur les forêts aléatoires pour segmenter la structure multicouche à 4 niveaux de la partie électrode-catalyseur des SOEC, et permettant d'évaluer quantitativement des paramètres microstructuraux importants comme la porosité et l'épaisseur. Le pipeline est conçu pour nécessiter un minimum de ressources informatiques et reste accessible même aux utilisateurs non spécialistes.

L'entraînement sur un jeu de données annotées représentatives des images FIB-SEM (10 images d'entraînement sur un total de 200) a permis d'atteindre une précision de segmentation de 68% sur l'ensemble données de test. Bien que cela indique la nécessité d'une amélioration supplémentaire, cela a été suffisant pour identifier des variations structurelles significatives. L'utilisation du pipeline sur plusieurs ensembles de données expérimentales FIB-SEM permet d'extraire des tendances statistiquement cohérentes en matière de porosité et d'épaisseur dans différentes conditions opérationnelles: cellules vierges (434 images), 100 heures (653 images) et 200 heures (484 images). La couche 4 a présenté une augmentation distincte de la porosité, tandis que la couche 2 affiche un changement remarquable en termes d'épaisseur.

Ces résultats montrent qu' une approche simplifiée d'apprentissage automatique combinée à un une approache traditionnelle de traitement d'image peut fournir des informations significatives sur les paramètres microstructuraux. Ils soulignent également le potentiel de développement d'un pipeline accessible et automatisé permettant d'évaluer quantitativement de larges jeux de données FIB-SEM de ces dispositifs électrochimiques en un temps record. Cependant, des améliorations potentielles pourraient également se porter sur le protocole d'annotation, l'ingénierie des caractéristiques et les approches combinées d'apprentissage automatique.

Mots-clés: FIB-SEM, analyse microstructurale, Random Forest, traitement d'images, électrolyse.

LIST OF ACRONYMS AND ABBREVIATIONS

AI : Artificial Intelligence

BMFTR : Federal Ministry of Research, Technology and Space

BPP : Bipolar Plates

CNN : Convolutional Neural Networks

DL : Deep Learning

FIB : Focused Ion Beam

GDC : Gadolinium-Doped Ceria

HER : Hydrogen Evolution Reaction

IPCC : Intergovernmental Panel on Climate Change

K-NN : K-Nearest Neighbors

LSM : Lanthanum Strontium Cobaltit

MEA : Membrane Electrode Assembly

MIEC : Mixed Ionic and Electronic Conductors

ML : Machine Learning

Nafion™ : Poly(tetrafluoroethylene-co-perfluoro-3,6-dioxa-4-methyl-7-octene sulfonic acid)

NASA : National Aeronautics and Space Administration

OER : Oxygen Evolution Reaction

PEMWE : Proton Exchange Membrane Water Electrolyzer

ScSZ : Scandia-Doped Zirconia

SEM : Scanning Electron Microscope

SOEC : Solid Oxide Electrolysis Cell

SVM : Support Vector Machine

WASCAL : West African Science Service Center on Climate Change and Adapted Land Use

YSZ : Yttrium-Stabilized Zirconium Oxide

LIST OF TABLES

LIST OF FIGURES

TABLE OF CONTENTS

GENERAL INTRODUCTION

GENERAL INTRODUCTION

Climate change is recognized as one of the greatest challenges for the 21st century, contributing to global warming and an increase in extreme weather events [1]. According to the Intergovernmental Panel on Climate Change (IPCC), global temperature could rise by 2 to 4°C by the end of the century if current trends persist [2].

One of the main drivers of this warming is the emission of greenhouse gases (GHGs), primarily from the combustion of fossil fuels. The anthropogenic emissions account for approximately 75% of the global GHGs, according to the International Energy Agency (IEA), raising major concerns about the sustainability of our energy systems [3]. In response, the international community has adopted landmark policies such as the Paris Agreement (2015), which aims to limit global warming to well below 2°C, ideally to 1.5°C [2] . In Europe, the European Green Deal sets an ambitious objective of carbon neutrality by 2050 through large-scale transformation of the energy, transport and industry sectors [4].

In this transition, hydrogen has emerged as a strategic energy vector. Its versatility allows for the decarbonization of hard-to-electrify sectors such as heavy industry, heavy transport and long-haul transport. The Global demand for hydrogen has reached a record of 95Mt in 2022 [4], and it is expected to exceed 100 Mt in 2025 according to the latest data from the International Energy Agency [5]. Yet, more than 95% of hydrogen is still produced from fossil fuels, mainly via steam reforming, generating substantial CO_2 emissions [6]. Green hydrogen produced through electrolysis of water using renewable electricity offers a low-carbon alternative. This method not only enables energy storage and grid flexibility but also paves the way for deep decarbonisation [7]. However, its large-scale deployment remains limited by high production costs, limited efficiency of electrolyzers and reliance on critical raw materials [8][9].

Among electrolyzer technologies, Proton Exchange Membrane Water electrolyzers (PEMWEs) and Solid Oxide Electrolysis Cells (SOECs) stand out. PEMWE systems operate at low temperatures, ranging from 50-80°C and offer a fast dynamic response. This makes them suitable for coupling with intermittent renewable energy sources [10]. Their drawback remains the use of expensive materials like platinum and iridium. In contrast, SOECs operate at high temperatures and achieve great energy efficiency up to 80% by exploiting thermal input. Their weakness lies in durability issues under real operating conditions, leading to performance degradation [11].

At the core of these performance and degradation phenomena lies the microstructure of the electrodes and electrolyte layers. Parameters such as porosity, tortuosity, and grain size directly influence layer properties, kinetic reaction and long-term stability [12]. Recent advances in high-resolution imaging techniques, particularly Focused Ion Beam-Scanning Electron Microscopy (FIB-SEM), now make it possible to visualize and reconstruct the complete 3D architecture of these materials at nanometer scales [13].

Yet, exploiting such images remains a challenge due to the structural complexity of the materials and the large volume of data generated. While advanced image analysis methods, including deep learning, can offer accurate results, they often require significant computational resources, expert knowledge and extensive annotated datasets [14][15]. This presents a major obstacle, particularly for non-experts or researchers without access to high-performance computing infrastructure.

To overcome this, the present work proposes the development of a simple, automated, and modular image processing pipeline that combines traditional processing methods with supervised machine learning. This approach is then applied to FIB-SEM images of SOEC electrodes to extract key descriptors such as porosity and thickness, enabling the evaluation of their evolution over operating time.

This thesis is structured in three chapters. Chapter 1 presents a critical review of the current state of hydrogen technologies, particularly SOEC and PEMWE, the challenges related to their materials, the importance of microstructural analysis and the theoretical framework for image processing. Chapter 2 describes the imaging protocol followed in this study. Chapter 3 discusses the results obtained from the processing pipeline and highlights the relevance of the approach for quantifying the key microstructural parameters.

CHAPTER 1: LITERATURE REVIEW

CHAPTER 1: LITERATURE REVIEW

In this chapter, we examine the existing literature related to the microstructural analysis and degradation mechanisms of SOECs and PEMWEs. We focus on the advancements in high-resolution imaging techniques, particularly FIB/SEM and their role in investigating the evolution of SOEC and PEMWE materials under operating conditions. Furthermore, we explore the developed quantification methods for microstructural parameters, ranging from the traditional approach to recent automated deep learning-based techniques.

1.1. Hydrogen Technologies

1.1.1. Solid Oxide Electrolysis Cells

- **History**

SOEC is an essential electrochemical technology for producing fuels such as carbon monoxide (CO) and dihydrogen (H_2), including syngas, from steam (H_2O) and/or carbon dioxide (CO_2) using electrical energy [16].

The history of SOEC began in 1899, with Nernst's discovery of the improved high-temperature ionic conductivity of doped oxides, specifically calcium-stabilized zirconia ($(ZrO_2)_{0.85}(CaO)_{0.15}$), which led to the "Nernst mass" [17] . This material was later used in 1962 to build the Solid Oxide Fuel Cell (SOFC), the inverse of the electrolyzer [17]. One of their experimental designs is shown in Fig.1.1, where a calcium-stabilized zirconia electrolyte tube and platinum electrodes were used in a high-temperature setup for fuel-water conversion. This early architecture laid foundational principles for modern SOFC and SOEC configurations. The first SOEC modeling studies, which took into account ohmic and concentration losses, were carried out in the late 1960s by H. Spacil and C. Tedmon in 1969 [18]. As of 1967, NASA (National Aeronautics and Space Administration) has also explored the use of these electrolytes for oxygen production and CO_2 utilization on space missions, and research, which is still ongoing [16]. In the 1980s, the German “Hot Elly” project marked a significant research and development effort, although it was halted in the 1990s due to low oil prices [19]. These developments represented milestones in the evolution of SOECs, paving the way for ongoing research focused on improving their efficiency, durability, and integration into modern energy systems.

Since the early 2000s, research on SOECs has progressed. New materials exhibiting improved

stability as well as ionic and electric conductivity, such as Lanthanum Strontium Chromium Manganese Oxide (LSCM), Lanthanum Strontium Manganite-Gadolinium-doped Ceria (LSM-GDC), have been investigated [19][20]. Research shifted toward reducing degradation and improving long-term performance [22]. In the 2010s, major EU-funded initiatives such as Horizon 2020 played a pivotal role in advancing SOEC technology. Projects like HELMETH,

GrInHy and REFLEX enabled the development and scale-up of high-temperature electrolysis systems, laying the groundwork for industrial demonstrations and long-term performance assessments [23]. Co-electrolysis of H_2O and CO_2 also gained attention and a pilot project validated the technology under real conditions [24][23]. Since 2020, efforts have been increasingly concentrated on lowering operating temperatures, using metal-supported cells, and improving electrode durability. SOECs are now tested for industrial integration in systems coupling renewable energy and carbon capture systems [25].

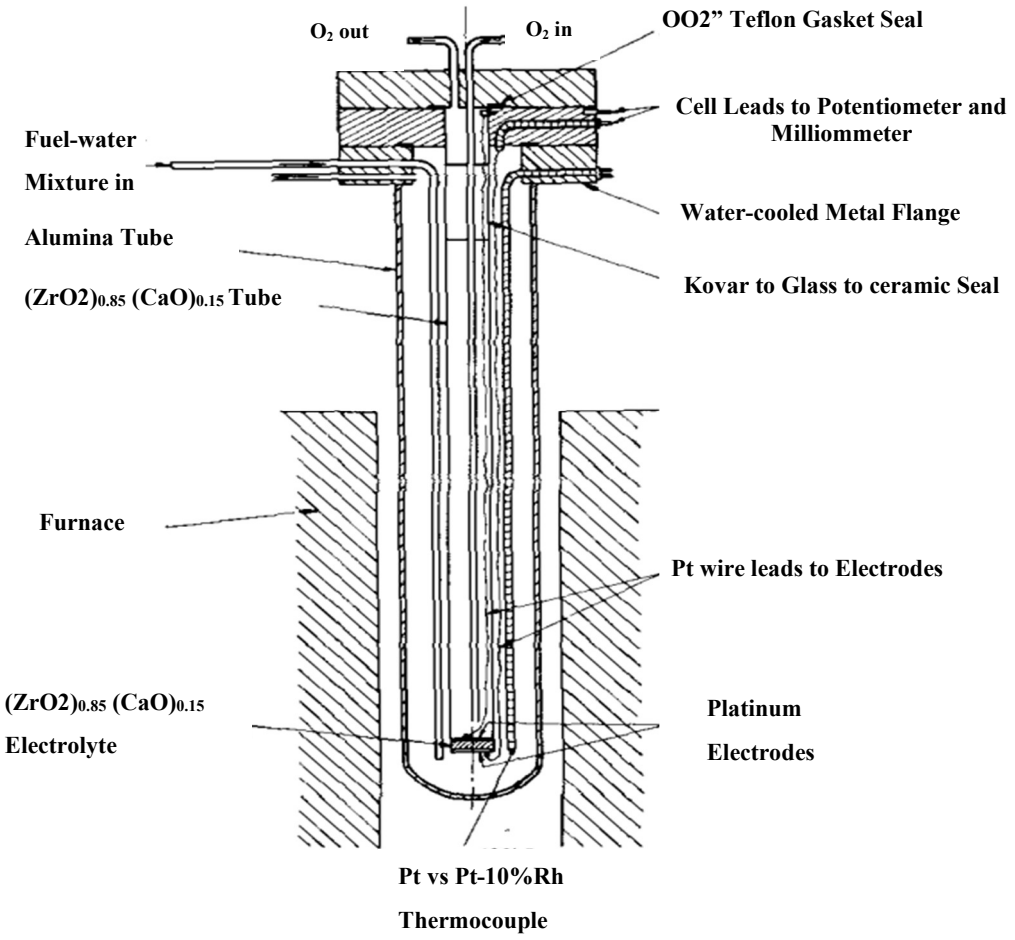

Figure 1.1. Schematic diagram of a galvanic cell with a solid oxide electrolyte [17]

- **Working principle**

An SOEC consists of three main components: 1) a hydrogen electrode (also known as the cathode), 2) an air electrode (also known as the anode) and 3) an electrolyte (a dense ceramic layer situated between two porous electrodes). However, unlike the SOFC, which converts the fuel to electricity, the electrochemical process in an SOEC operates in reverse mode to produce hydrogen from water.

During operation, electrons are supplied by the external power source at the hydrogen electrodes, where water vapor is also introduced. The water breaks down into dihydrogen (H_2) and oxide ions (O^{2-}). The oxide ions migrate through the dense electrolyte and reach the air electrode, where they are oxidized to form molecular oxygen, releasing electrons into the external circuit, thereby completing the electrochemical loop [26][27]. Fig.1.2 illustrates the structure in operation mode.

The overall electrochemical reaction equation is as follows:

Cathode Reaction: $H_2O_{(g)} + 2e^- \rightarrow O^{2-} + H_{2(g)}$ (1)

Anode Reaction: $O^{2-} \rightarrow 1/2\, O_{2(g)} + 2e^-$ (2)

Overall equation: $H_2O_{(g)} \rightarrow H_{2(g)} + 1/2\, O_{2(g)}$ (3)

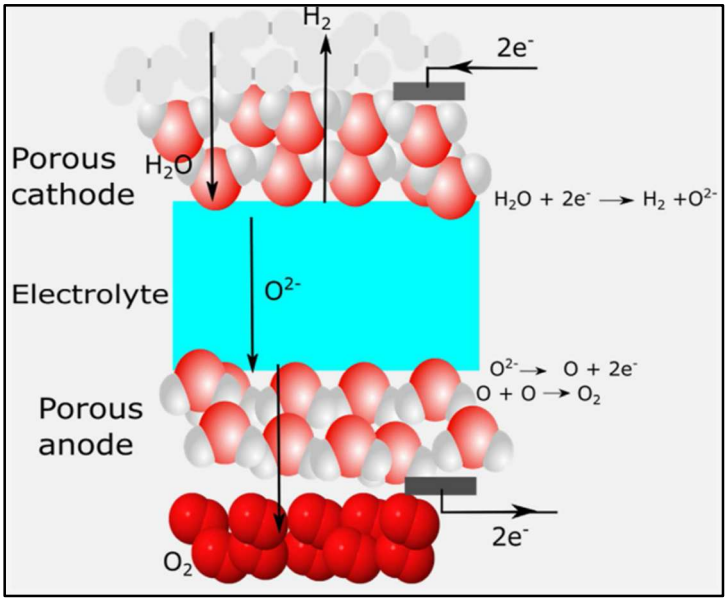

Figure 1.2. Fundamental working principles of SOEC [26]

- **Materials and Architecture of SOEC Components**

The development of SOECs relies heavily on the selection and optimization of functional materials for each cell component. These materials must meet several essential requirements. They should exhibit adequate porosity to ensure effective gas penetration and high conductivity (both ionic and electrical) to enable charge transfer [28][12]. In addition, chemical compatibility is essential to avoid undesirable reactions with other cell components [29]. Lastly, the thermal expansion coefficient must be compatible with the rest of the cell to prevent mechanical stress during temperature variations [30].

This section takes a closer look at the primary materials currently used and under investigation for electrodes and electrolytes, as well as their challenges and potential.

a) Hydrogen Electrode (Cathode)

The hydrogen electrode, serves as the reactive site where the water splitting reaction takes place. It plays a critical role in SOEC operation, notably by facilitating the adsorption of water vapor, its activation on catalytic sites, and the efficient evacuation of the hydrogen produced. Nickel (Ni) is the most commonly used material due to its excellent electronic conductivity and satisfactory catalytic activity [31]. However, pure nickel has a high thermal expansion coefficient (16.9×10^{-6}/°C at full density), which leads to poor mechanical compatibility with the electrolyte, especially when it is yttrium-stabilized zirconium oxide (YSZ). To address this issue, Ni-YSZ cermet is used, where the ceramic matrix helps to match the thermal behavior of the electrolyte, thereby reducing the stress and risk of failure [32]–[34]. An alternative to Ni-YSZ is the nickel-based gadolinium-doped ceria (Ni-GDC), which shows improved chemical stability at lower temperatures. However, it suffers from phase interaction that degrades performance over time. More advanced materials like ($La_{0.6}Sr_{0.4}Cr_{0.2}Mn_{0.8}O_3$, LSCM), which are mixed ionic and electronic conductors (MIECs), have demonstrated better thermal stability and resistance to oxidation [12]. Today, techniques like nanoparticle infiltration boost catalytic activity and the triple-phase boundary (TPB) density. However, keeping these properties stable at high temperatures and long operation is difficult [35].

b) Air Electrode (Anode)

The air electrode is the site of the oxygen evolution reaction (OER). It plays an important role

in the electrochemical reaction process by facilitating oxide ion access to catalytic sites and by-product removal via its porous structure.

At the state of the art, materials such as lanthanum strontium manganite-yttria stabilized zirconia composites (LSM-YSZ), as well as MIECs materials such as lanthanum strontium cobalt ferrite ($La_{1-x}Sr_xCo_{1-\gamma}Fe_\gamma O_{3-\delta}$, LSCF) or other perovskite-based materials, are predominantly used for the anode [36]. Research is currently focused on exploring different types of materials to improve the performance of anode electrodes. Among the most studied materials are double perovskites and Ruddlesden-Popper (RP) materials, which offer a good compromise between electrical conductivity, chemical stability and compatibility with other cell components. The structure is shown in Fig.1.3 [12].

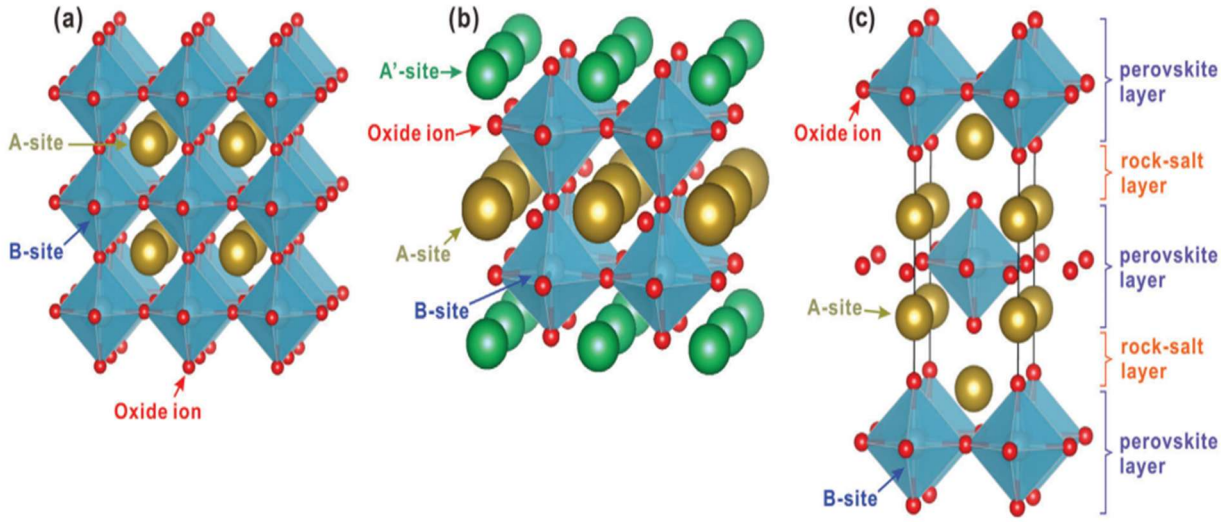

Figure 1.3. Illustration of the crystal structures of: a) perovskite, b) double perovskite, and c) Ruddlesden-Popper (RP) perovskite [37]

c) The Electrolyte

The main function of the electrolyte is to transport oxide ions (O^{2-}) between the anode and cathode, enabling the electrochemical reaction required for high-temperature hydrogen production.

The performance of an electrolyzer depends on its capacity to facilitate rapid oxide ion conduction while preventing electron transfer to guarantee an efficient electrochemical reaction. Among the electrolyte materials used in SOECs, two prominent families are commonly studied: yttria-doped zirconia (YSZ) and scandia-doped zirconia (ScSZ). YSZ is the

more traditional material, due to its thermal stability. It offers good oxide ion conductivity, especially between 700-900°C, although its performance tends to decline below 700°C, which may limit its efficiency for intermediate temperature operation. In contrast, ScSZ offers superior conductivity and operates at slightly lower temperatures, especially around 600°C, which is advantageous for reducing power consumption and extending cell life [24][38].

Ceria-based electrolytes, such as gadolinium-doped ceria (GDC), are also considered promising for intermediate-temperature applications. The material exhibits higher ionic conductivity than YSZ between 550-700°C, but suffers from a critical drawback in a reducing environment, as Ce^{4+} tends to be reduced to Ce^{3+}, including unwanted electronic conductivity and possible mechanical instability [39] [40]. Finally, other materials like lanthanum gallate ($LaGaO_3$) have also attracted attention thanks to their excellent ionic conduction, but their chemical stability has yet to be confirmed in specific environments [12]. While some materials perform well, there is still a need for new materials to enable large-scale use.

1.1.2. Proton Exchange Membrane Electrolyzer

- **History**

PEMWE originated from research into PEM fuel cells in the 1960s, notably as part of NASA's Gemini space program. At that time, Grubb and Niedrach at General Electric developed the first cells to use a polymer membrane to conduct protons, laying the foundations for today's PEM electrolysis concept [41].

A decisive turning point came in 1968 with the commercial introduction of Nafion™ (Poly(tetrafluoroethylene-co-perfluoro-3,6-dioxa-4-methyl-7-octene sulfonic acid)), a perfluorosulfonic polymer developed by DuPont. This material offered excellent proton conductivity, high chemical resistance, and thermal stability, enabling the realization of prototype electrolyzers operating at moderate temperatures, 60-80°C, with high purity of the gas produced [42].

In 1973, J.H. Russell published the first detailed study of a PEM electrolyzer, demonstrating promising performance with current densities of the order of 1 A/cm² at 1.88 V [43]. These results confirmed the advantage of this technology over traditional alkaline electrolyzers [43].

In the 2000s, interest in PEMWEs was revived by advances in membrane durability, catalyst

stability, and overall performance. Research intensified in reducing the quantity of noble metals (iridium, platinum), developing alternative membranes such as Sulfonated Polyether ether ketone (SPEEK), and optimizing electrode architectures [44][10].

Today, PEMWEs are considered a key technology for producing green hydrogen, especially in Power-to-Gas systems and in the integration of renewable energy. Their low-temperature operation, compactness, and rapid response capability make them a suitable solution for decentralized applications. However, challenges remain, notably related to material durability, catalyst cost, and large-scale industrialization [45]–[47].

- **Operating Principle**

The main purpose of the PEMWE is to convert electrical energy into chemical energy, specifically hydrogen. Before exploring the individual components of the cell, it is useful to understand how the cell works.

In this electrochemical process, clean water is provided to the anode side. When a voltage is applied to the electrodes, the water undergoes oxidation in a process known as the Oxygen Evolution Reaction (OER), generating protons (H^+), dioxygen (O_2), and electrons. The generated protons migrate through the proton exchange membrane electrolyte toward the cathode side, where they are reduced (Hydrogen Evolution Reaction, HER) by combining with electrons to form hydrogen (H_2) [48], as shown in Fig.1.4. The overall electrochemical reaction equation is as follows:

Anodic reaction:	$H_2O \rightarrow 2H^+ + 1/2\ O_2 + 2e^-$	(1)
Cathodic reaction:	$2H^+ + 2e^- \rightarrow H_2$	(2)
Overall reaction:	$H_2O \rightarrow H_2 + 1/2\ O_2$	(3)

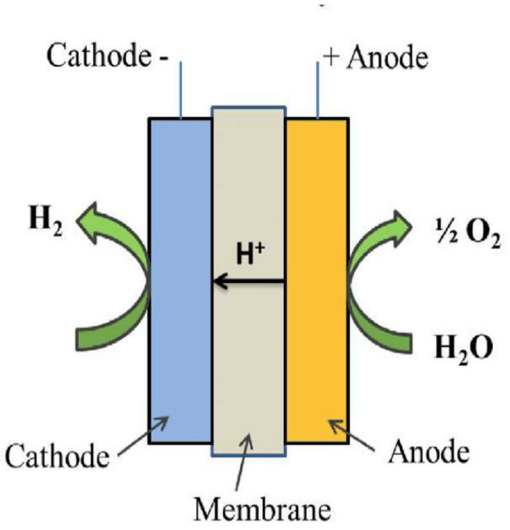

Figure 1.4. Schematic illustration of PEMWE, adapted from [49]

Although this process may seem straightforward, in the background, the microstructure properties of the materials involved highly affect the efficiency and durability of the system [50]. Therefore, a detailed examination of the cell's structural components is essential for a deep understanding of how the material properties influence overall performance.

- **Structure and Layer Architecture**

A standard PEMWE comprises several key components, including the bipolar plates (BPP), the current collectors, and the membrane electrode assembly (MEA). Fig.1.5 gives a general overview of the system.

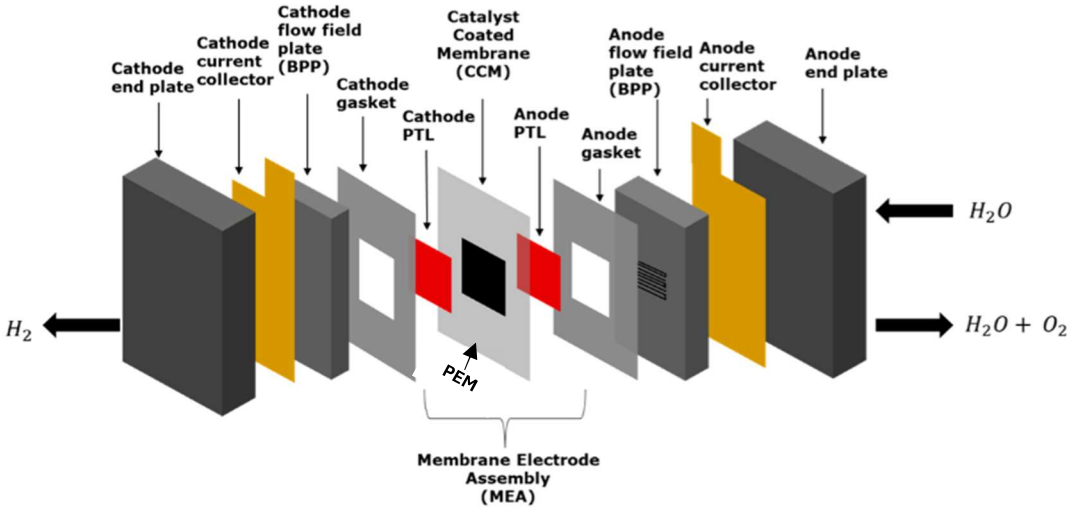

Figure 1.5. Schematic view of PEMWE cell architecture [51]

- **Bipolar Plates (BPPs)**

Bipolar Plates are flat components located between neighboring cells in the stack, forming the structural backbone of the electrolysis cell. Generally made of titanium, their primary roles involve the transport of water within the cell, facilitating gas removal, regulating heat exchange and closing the external electrical circuit [52]. Titanium is widely used as a material due to its excellent thermal conductivity, mechanical strength, and corrosion resistance. Nonetheless, in the highly oxidative anodic environment, titanium is prone to corrosion, leading to cell deterioration. Despite the investigation of different coatings and alloys to tackle this problem, their high cost makes them unsuitable for large-scale applications [49].

- **Current collectors**

The current collector is a porous conductive layer located between the electrode's catalyst layer and the bipolar plate. To effectively perform, it needs to provide excellent electrical conductivity and resistance to corrosion, especially on the anode side. Its microstructure requires careful refinement and should be designed to strike a balance between high porosity to eliminate gases, but excessive porosity can reduce the electronic conduction and limit water supply to catalytic sites. This remains one of the key challenges in enhancing the overall efficiency of the cell [52].

- **Membrane Electrode Assembly (MEA)**

The MEA is the primary functional unit of PEMWE, where essential electrochemical reactions occur, transforming electrical energy into chemical energy. It comprises three closely bonded parts: 1) the anode, 2) the cathode, and 3) the Proton Exchange Membrane (PEM).

1) The anode

The porous structure of the anode usually includes iridium-based catalysts such as Iridium (Ir), iridium oxide (IrOx), or iridium ruthenium oxide (IrRuOx) combined with an ionomer, a proton-conducting polymer often derived from Nafion and interconnected. These structural elements are essential for mass transport and ion conduction but can also cause conversion losses, mainly due to limited reagent access and uneven catalyst utilization. The porous design directs the movement of reactants and products and determines how well the catalyst can be accessed. The anode affects overall efficiency and can help decrease the amount of costly

catalyst needed if its structure is optimized.

A critical parameter is the triple-phase boundary (TPB), where electrons, ions, and gaseous molecules interact. Maximizing the interface area while minimizing ohmic and mass transfer resistances can significantly improve performance. Strategies such as graded porosity, controlled ionomer distribution, or nanostructuring are being actively explored to increase catalytic efficiency and reduce the amount of iridium used, as this metal is expensive and scarce [53][54].

2) Cathode

On the cathode side, the HER is kinetically more favorable. A platinum-based catalyst supported on carbon is generally used for this reason. This setup provides good electrical conductivity and fast reaction rates. However, long-term stability remains a challenge, mainly due to the corrosion of the carbon support in acidic and humid environments. Research is ongoing to replace carbon with other materials or to develop more resistant platinum alloys[55].

3) Pronton Exchange Membrane (PEM)

The proton exchange membrane (PEM) serves two main functions: it conducts protons (H^+) from the anode to the cathode and acts as a gas barrier, preventing hydrogen and oxygen from mixing. Nafion, is the most commonly used material because of its high ionic conductivity, chemical resistance, thermal stability, and mechanical strength [56], as shown in Fig.1.6.

Despite its excellent properties, Nafion has certain limitations, notably high current density drying and high cost. As a result, alternatives are being investigated, such as hydrocarbon-based membranes, for example, Sulfonated Polyether ether ketone (SPEEK) or composite membranes incorporating inorganic fillers. These materials aim to improve moisture retention, durability, and reduce costs, while maintaining good conductivity [57][58].

Membrane thickness and hydration state have a strong influence on ionic resistance. Thinner membranes reduce ohmic losses, but increase the risk of gas cross-permeation. It is therefore crucial to strike a balance between electrochemical performance and safety [59].

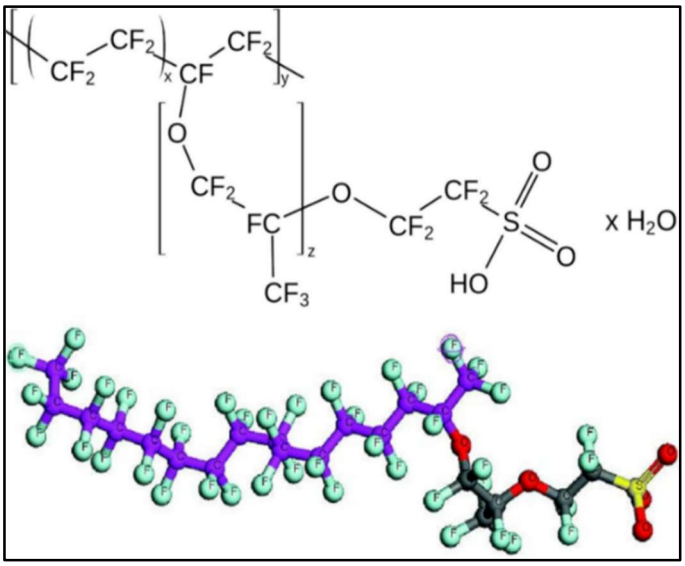

Figure 1.6. Molecular structure of Nafion [52]

1.2. Challenges and Degradation Mechanisms Affecting SOEC and PEMWE Performance

Although material selection is critical to SOEC and PEMWE performance, it is equally important to understand how these materials degrade under real operating conditions. Chemical degradation mechanisms such as electrode corrosion and unwanted phase formation have been extensively investigated. Increasing attention is also being given to physical degradation processes, including thermal cycling, mechanical stress, and microstructural evolution [55][60]. Both forms of degradation, often interconnected, significantly affect the long-term stability and efficiency of the cells. This section examines some key structural degradation mechanisms.

1.2.1. Particle coarsening

Ananyev *et al.*[61] investigated the evolution of particle coalescence in LSM-YSZ cathodes over time. The physical degradation mechanisms in these cathodes were analyzed to quantify the impact of particle coalescence on the material's microstructure under high-temperature operating conditions. Microstructure images were obtained by scanning electron microscopy (SEM). These images were then analyzed using a semi-automated pipeline based on grayscale histogram segmentation, enabling the evolution of porous and solid phases to be tracked over time.

The results shown in Fig.1.7 reveal an exponential growth in the degraded zone, marked by

particle coalescence and decreased porosity. This morphological change causes a decline in electrochemical performance due to increased tortuosity and a reduction in the active specific surface area. Although research on electrode particle growth has primarily focused on solid oxide fuel cells (SOFCs), these mechanisms also occur in SOECs, since both systems operate at similar temperatures and involve comparable sintering and particle coalescence processes. However, it is important to note that some phenomena related to polarization and element displacement might vary depending on the operating mode.

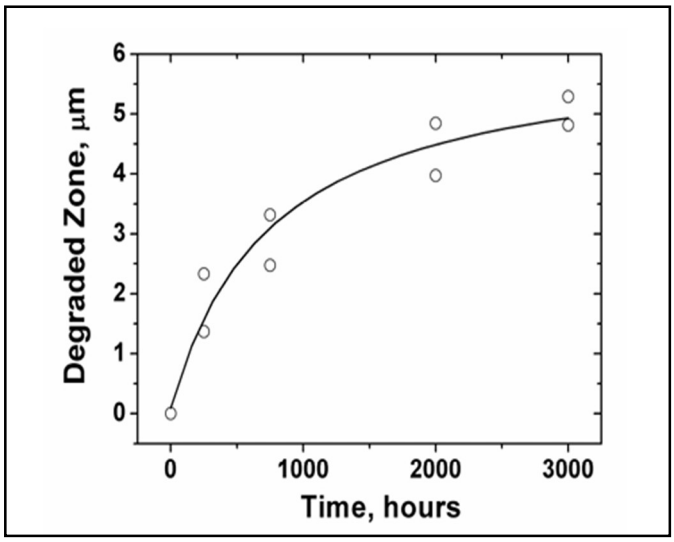

Figure 1.7. Evolution of the degradation zone thickness over time [61]

1.2.2. Porosity changes during redox cycling

To evaluate the impact of porosity evolution on the degradation process, a study was conducted by De Angelis *et al* [62]. Researchers used nanotomographic X-ray ptychography to examine the microstructural evolution of Ni-YSZ electrodes subjected to a complete redox cycle. They aimed to understand how the fragmentation of nickel particles and the formation of internal voids influence the porous microstructure. They were particularly interested in pore volume and connectivity, which are essential for cell performance at high temperatures. High-resolution 3D reconstruction enabled precise visualization of pore morphology, Ni particles and NiO phases. These observations were made before, during and after redox cycling.

The results show a significant decrease in the average pore radius, which drops from around 350 nm to 100 nm. This indicates considerable fragmentation of the pore network. On the other

hand, pore connectivity increases from 90% to 99% demonstrating the formation of new porous pathways, caused by the fragmentation of nickel particles. These microstructural changes lead to a deterioration in electrochemical performance, which can also increase mechanical deterioration. Thus, particle fragmentation and pore migration illustrate how the redox cycle degrades microstructures and affects cell lifespan.

1.3. Microstructural Characterization Techniques

1.3.1. Overview of microstructural characterization techniques

Techniques for microstructural characterization are important for analyzing catalytic materials and electrodes, providing spatial detail regarding the internal structure [63] .

Two-dimensional (2D) techniques, such as scanning electron microscopy (SEM), transmission electron microscopy (TEM), and electron backscatter diffraction (EBSD), often used as a detector in SEM, allow detailed analysis of the local morphology, nano-to-microscale phase distribution and crystallographic orientation [64][15]. However, their main limitation is their inability to provide complete volumetric and topological information. To estimate three-dimensional (3D) microstructural parameters, researchers traditionally used geometrical models such as the general effective medium (GEM), the concept of contiguity (CC), the random network model (RNM) and the random packing sphere model (RPSM). These models rely on strong assumptions, for example, the random mixture of sphere particles, meaning the material is approximated as randomly packed spheres. This assumption may bias the interpretation of microstructure-related properties [65].

To achieve this, 3D techniques such as FIB-SEM, nano to micro-CT X-ray tomography, and electron tomography provide detailed visualization of the porous network, interfaces, and internal topology at nanometric and micrometric scales [66].

These volumetric approaches foster a thorough understanding of porous connectivity and transport pathways, which are essential for optimizing the performance of catalysts and electrode materials. Fig.1.8 illustrates the increasing interest in 3D characterization techniques, comparing their capabilities in terms of spatial resolution and sample volume analyzed:

However, the FIB-SEM tomography technique has recently attracted growing interest within the scientific community. This is primarily due to its unique ability to provide high-resolution,

three-dimensional visualization of complex structures, as well as to accurately quantify porous topologies, interfaces, and the connectivity of catalytic materials and electrodes. These features make it an essential tool for in-depth analysis of structure-performance relationships [67].

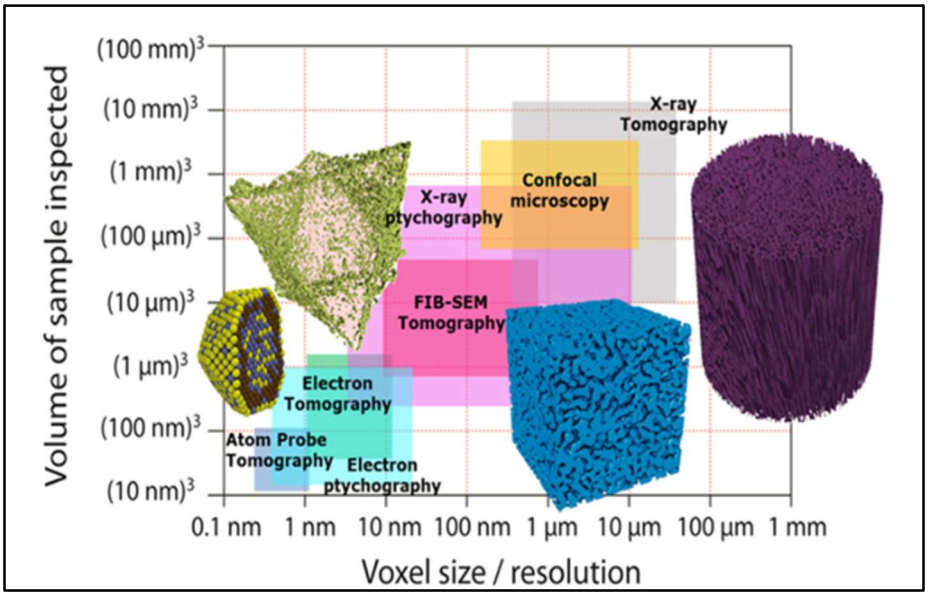

Figure 1.8. Tomographic imaging methods by resolution and volume range [64]

1.3.2. Focused Ion Beam - Scanning Electron Microscope (FIB-SEM)

The technique combines the use of FIB and SEM. The FIB targets the sample surface and performs controlled ablation by slicing the material into a series of nano-sized layers, revealing new cross-sections. Simultaneously, SEM captures high-resolution images of each newly exposed surface, enabling precise three-dimensional reconstruction of the sample's microstructure [67]. See the illustration in Fig.1.9.

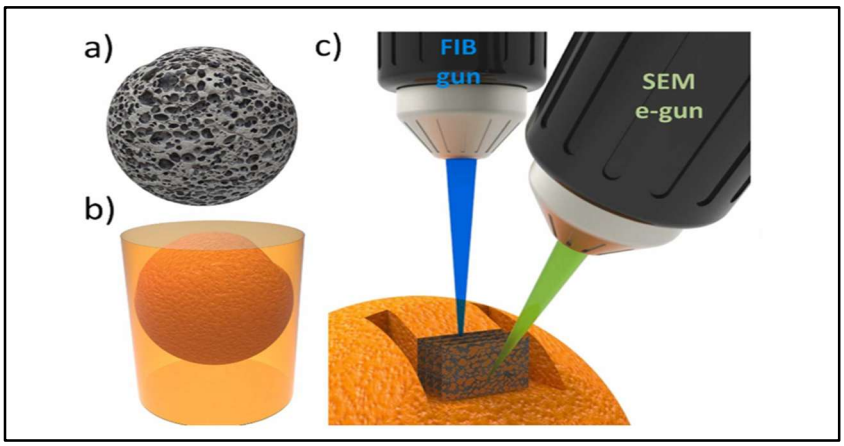

Figure 1.9. Illustration of the steps and principles of the FIB-SEM tomography process applied to a porous material: a) Porous structure, b) Embedded in resin to prevent artefacts during the imaging process, c) FIB-SEM slice and image process on trimmed surface [64]

After acquiring three-dimensional microstructural images, a pre-processing and segmentation process is performed to accurately distinguish the different microstructural phases. More than just a technical tool, it serves as a bridge between raw visual data and scientific interpretation.

1.4. Image processing and quantification approaches: from traditional methods to deep learning-based quantification

Image processing involves a set of techniques used to analyze and extract useful information from visual data. As shown in Fig.1.10, it includes tasks such as segmentation, image generation and object detection [68].

These techniques generally fall into two categories: traditional methods based on conventional algorithms [69] and modern approaches based on artificial intelligence (AI), particularly Machine Learning (ML) and Deep Learning (DL). The latter provides enhanced accuracy and new opportunities for complex image analysis tasks [70][71].

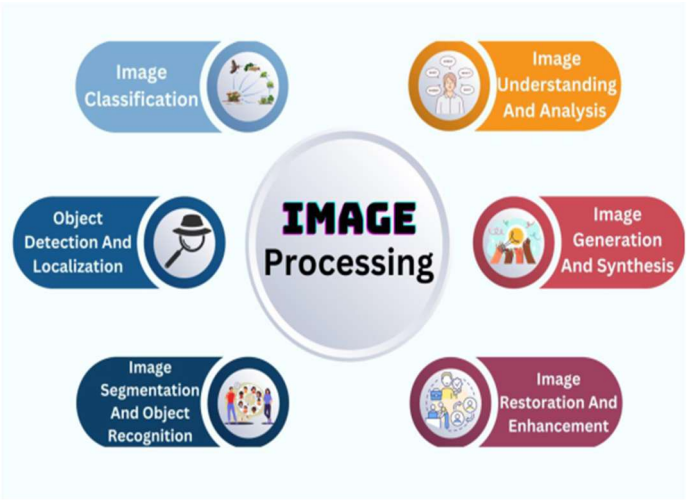

Figure 1.10. Different types of image processing [68]

1.4.1. Traditional Approaches: Case Study

In the microstructural analysis of the catalyst layer, precise phase segmentation is critical for reliably quantifying key parameters such as porosity and grain size. Historically, deterministic rule-based methods relying on thresholding have been widely used. For example, Ananyev *et al* [61] implemented the classical Otsu-based approach, combined with Gaussian curve approximation, achieving improved phase separation compared to employing each technique separately, as summarized in Fig.1.11 and Fig.1.12.

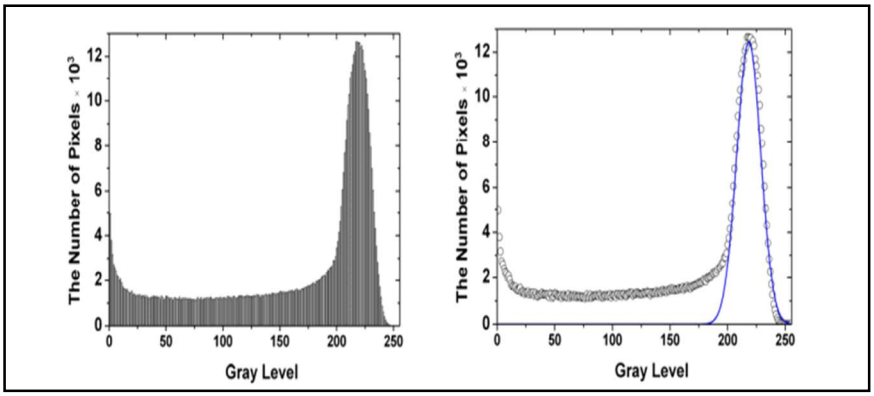

Figure 1.11. Grey level histogram and Gaussian curve distribution [61]

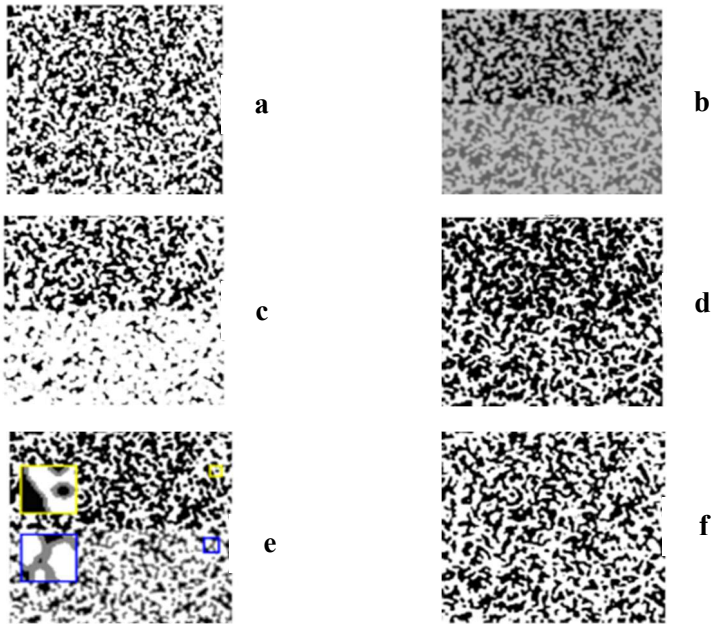

Figure 1.12. Comparison of image processing steps for microstructure segmentation: a) Original image, b) Smooth image, c) Otsu method, d) Gaussian approach, e) Analysis of the segmented area, f) Combination of Otsu and Gaussian methods [61]

1.4.2. Deep Learning-Based Segmentation: Case Study

Advanced deep learning (DL) techniques, such as semantic segmentation networks, U-Net, and DeepLabV3, are increasingly adopted for microstructure quantification. Hwang *et al* [72] demonstrate the efficacy of the DeepLabV3, a CNN-based architecture, for segmenting microstructural images of fuel cell electrodes. This model enables precise delineation of different phases, such as Ni and YSZ. Validation results, Fig.1.13, confirmed reliable segmentation accuracy, which is highly dependent on the quantity of annotated training data. Thus, good quality labeled data is key for precise deep learning results.

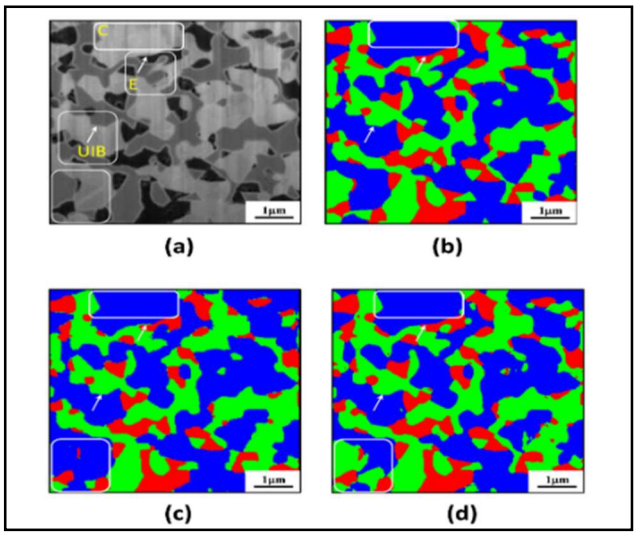

Figure 1.13. Comparison of ground truth and Deep Learning segmentation results: a) original image, b) ground truth image, c) Deep learning prediction on improperly prepared ground truth, d) DL prediction on properly prepared ground truth [72]

1.4.3. Quantitative Microstructure Analysis Approach

Quantitative microstructure analysis represents an important step for characterizing electrochemical materials. Traditionally, manual or semi-automatic stereological methods, such as linear intercept, have been used. For instance, Bae *et al*, [73] employed this approach to measure the volume fractions of pores, LSM, and GDC in a composite cathode by overlaying intersection lines on micrographs and counting phase intersections as illustrated in Fig.1.14. To convert measured lengths into volume estimates, the assumption of isotropy of the microstructure is often made; in other words, properties are assumed to be the same in all directions. This assumption makes it possible to relate 2D measurements to 3D characteristics. However, this assumption is not always valid, particularly in the case of anisotropic materials, which can introduce interpretation bias. In addition, these methods often suffer from poor reproducibility, time-consuming manual processing, and difficulty in estimating parameters such as tortuosity, which refers to the complexity of the path inside the porous structure [73].

These limitations drove the development of more advanced methods based on digital image processing and programming tools shuch as Python. These modern approaches offer automated, reproducible analysis of key features.

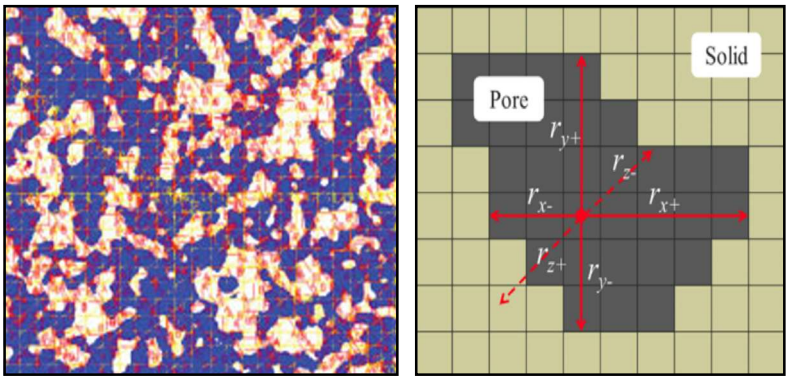

Figure 1.14. Schematic illustration for the linear intercept method for pore structure quantification [73]

1.5. Theoretical foundation of Image processing

The following section presents the theoretical foundations of image processing, offering an overview of essential techniques that encompass both traditional methods and modern approaches introduced earlier.

1.5.1. Fundamentals of Traditional Image Segmentation Approaches

Traditional image segmentation typically follows a sequence of stages designed to enhance image quality, identify relevant structures and accurately delineate regions of interest.

Table 1.1 below summarizes the main phases and components commonly found in these processes. It provides a concise framework for the detailed overview.

Table 1. 1. Concise summary of image processing stages

Phase	Component	Task	Reference
Pre-processing	Image registration	Align the images by correcting shifts	[74]
	Noise reduction	Reduce noise without losing important details	[75]
	Contrast enhancement	Improve visibility of structures of interest	[76]
Segmentation	Thresholding-based segmentation	Separate regions based on pixel intensity levels	[77]
	Region-based segmentation	Group homogeneous and spatially connected zones	[78]
Post-processing	Morphological operation	Refine and correct segmented masks	[79]

A: Image pre-processing

Image pre-processing aims to prepare raw images for analysis by enhancing their quality. Steps like noise reduction, artifact correction help ensure that all following measurements and segmentations are based on clear and reliable data.

A1: Image registration

Image registration is a preliminary step aimed at spatially aligning multiple images of the same scene. Particularly in FIB-SEM, during acquisition, small shifts in X and Y directions may occur due to differences in alignment or perspective. To address these issues, image registration methods detect characteristic points and apply geometric transformations. This enables an accurate overlay of images for consistent analysis [80][74].

A2: Noise reduction

This stage aims to minimize the random noise and irregularities introduced during image

acquisition without affecting key structures. It provides a more reliable foundation for later analysis. Specific filters are used to reduce these imperfections [75]. Among them, the Gaussian filter and the Median filter are commonly used for this purpose.

Gaussian filter: This method is designed to remove diffuse noise, resulting in a smoother image. It works by applying a convolution with a Gaussian kernel, where the sigma parameter controls the level of blurring, see Fig.1.15. A small sigma retains more detail, while a larger value produces smoother results by reducing local intensity variations based on pixel proximity [81].

The following equation defines the two-dimensional Gaussian kernel used for this operation [82]:

$$G(x) = \frac{1}{2\pi\sigma^2} \exp\left(-\frac{x^2 + y^2}{2\sigma^2}\right) \quad (1)$$

Where sigma (σ) determines the degree of smoothing.

The variables x and y represent the coordinates that show how far a point is from the center of the Gaussian curve, used to calculate the smoothing effect.

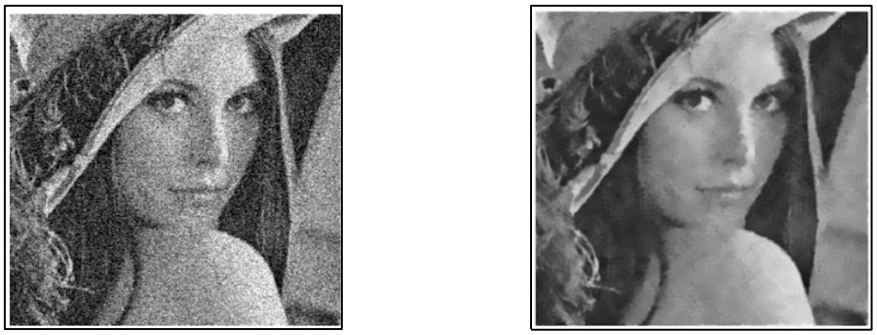

a b

Figure 1.15. Illustration of an image with Gaussian noise (a) and its denoised version (b)[83]

Median filter: The median filter is particularly effective against impulsive noise, also known as "salt and pepper" noise, which appears as randomly distributed very dark or very bright pixels. This filter reduces noise while preserving structural details, such as edges (see Fig.1.16), unlike the Gaussian filter, which tends to smooth fine details. It involves replacing each pixel with the median value of neighboring pixels within a local window, also known as a kernel [84].

Mathematically, for a given pixel at position (m, n) in the image, the median filtered value $P_s(m, n)$ $u$sing a window of size $s \times s$ defined as [85]:

$$\boldsymbol{P_s\,(m,n) = median_s[p(i,j)]} \qquad \mathbf{2}$$

Where $i\ and\ j$ are the indices of the neighboring pixels in the kernel window around the pixel (m,n).

$$\boldsymbol{i \in \left(m - \frac{s-1}{2}, \ldots, m + \frac{s-1}{2}\right)\ an\ j \in \left(n - \frac{s-1}{2}, \ldots, n + \frac{s-1}{2}\right)} \quad \mathbf{3}$$

This means that the new value of the pixel (m, n) is the median of all pixel intensities $p(i, j)$ within a square neighborhood of size $s \times s$ centered at (m, n)

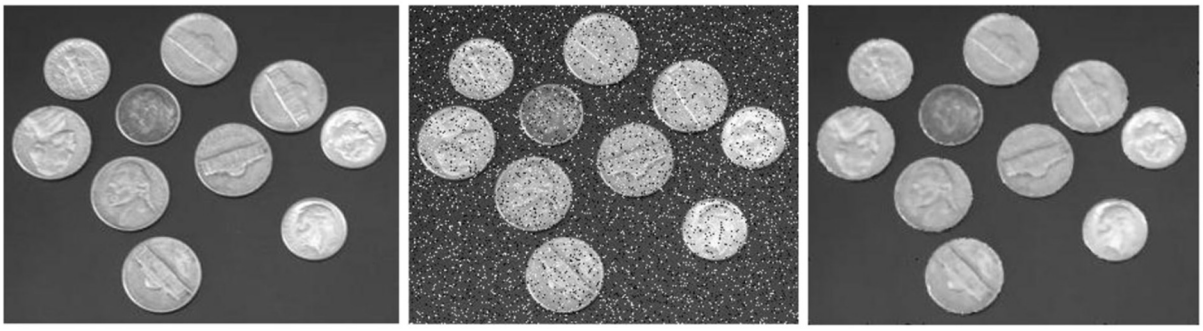

a **b** **c**

Figure 1.16. Comparative illustration of the effects of noise on an image and its filtering: a) Original image, b) Image polluted by salt and pepper noise, c) Image after median filtering with a window size of 3× **3** [86]

A3: Contrast enhancement

Visual perception and subsequent segmentation are greatly enhanced by this step, making structures that are difficult to see in the initial image more noticeable [76]. Some of the classic methods used include: Contrast Limited Adaptive Histogram Equalization (CLAHE) and Unsharp Mask.

CLAHE: The CLAHE method improves the image contrast while preventing oversaturation in bright areas. The image is typically divided into small tiles, and histogram equalization is

applied locally with a clip limit to control contrast amplification. Locally, the histograms are clipped according to the following rule [87]:

$$\mathbf{H_i(g) = min(H(g), C)} \quad \mathbf{4}$$

Where $H(g)$ is the original histogram for gray level g, $C$is the clip limit, and $H_i(g)$ is the clipped histogram

Unsharp Mask: Unsharp mask improves contrast and sharpens the image by subtracting a blurred version from the original and then adding the difference back [88].

B: Image segmentation

Segmentation refers to dividing an image into distinct regions or objects, making it easier to identify and study specific structures. By isolating relevant features, it provides a solid foundation for accurate measurement and meaningful comparisons.

B1: Thresholding segmentation

Thresholding segmentation analyzes pixel intensity histograms to find one or more optimal thresholds that separate different pixel classes. These methods include binary, multi-level and adaptive thresholding. These are simple yet effective for segmenting objects from the background, especially when intensity differences are prominent.

Global threshold (binary) assigns a pixel based on a single fixed or automatically determined threshold. A widely used algorithm for automatic global thresholding is Otsu's method, see Fig.1.17, which automatically finds the optimal threshold by minimizing the intra-class variance, or equivalently, by maximizing the inter-class variance, based on the intensity histogram [89][90] the intra-class variance is defined as:

$$\boldsymbol{\sigma_w^2(t) = \omega_0(t)\sigma_0^2(t) + \omega_1(t)\sigma_1^2(t)} \quad \mathbf{5}$$

The inter-class variance is defined as:

$$\boldsymbol{\sigma_b^2(t) = \omega_0(t)\omega_1(t)\big(\mu_0(t) - \mu_1(t)\big)^2} \quad \mathbf{6}$$

Where $\omega_0(t)$ and $\omega_1(t)$ are the probabilities of the two classes of pixels, $\sigma_0(t)$ and $\sigma_1(t)$ are the variances of pixel intensities of each class, and $\mu_0(t)$ and $\mu_1(t)$ are the mean intensities of each class. The optimal threshold (t) is the value that maximizes $\sigma\_b^2(t)$, ensuring the best possible separation between the two classes.

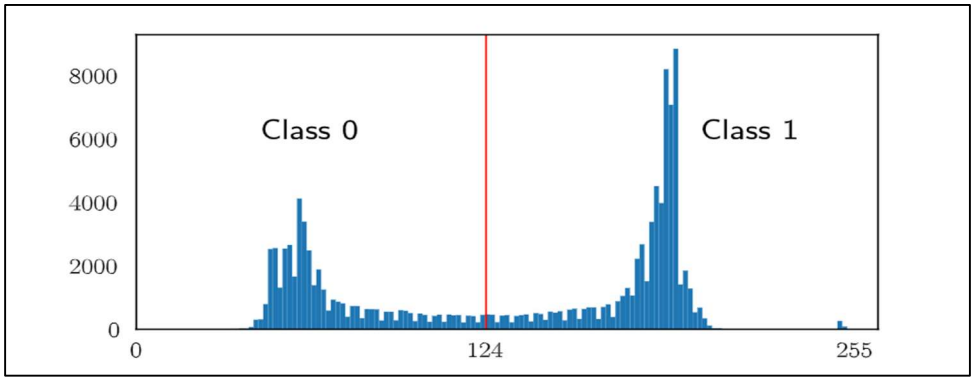

Figure 1.17. Segmentation using Otsu's thresholding [91]

Multi-threshold extends this approach to segment multiple classes by finding several optimal thresholds, as depicted in Fig.1.18. The multi-level version of Otsu's method, known as Multi-Otsu, can be used for such cases.

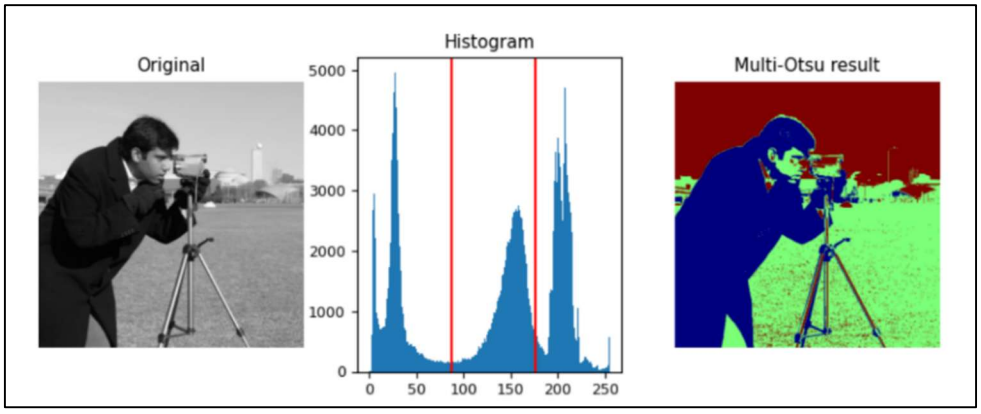

Figure 1.18. Image segmentation using Multi-Otsu thresholding [92]

B2: Region-based segmentation

These steps group pixels into regions based on their local homogeneity and spatial connectivity by identifying areas in the image that share similar characteristics. They are handy for distinguishing between adjacent or overlapping objects, even when there is no sharp difference in intensity [15]. Among the existing methods, Watershed and Region growing are well known.

Watershed algorithm: This algorithm interprets the image as a 3D landscape and floods it from the lowest pixel intensity points to separate different objects. Before applying the algorithm, edge detection methods like Sobel or Canny can be used to better define boundaries and guide the separation [71] [93].

Region Growing: It is a segmentation method that for regions by grouping neighboring pixels with similar characteristics, starting from selected seed points. This approach is particularly useful for segmenting objects with gradual intensity variations [78].

C: Morphological post-processing

After the segmentation, morphological operations are utilized to refine the outcomes by closing small gaps, splitting or merging objects and eliminating any residual noise. Opening and closing are the most commonly employed operators in this context.

Opening: An erosion operation followed by a dilation process that effectively removes small, isolated noise objects while preserving the overall shape of the segmented regions [94].

Closing: Consists of dilation followed by erosion, it is used to fill small gaps or spaces in segmented objects and bring close elements together to ensure continuity [15].

These traditional image processing methods are still important; they improve image quality and provide a solid foundation for advanced approaches.

1.5.2 Artificial Intelligence

Artificial intelligence is a branch of computer science that develops systems capable of mimicking certain human cognitive functions, such as learning, reasoning, and decision-making. It has a wide range of applications, including language processing, image analysis, and robotics. Today, AI is increasingly recognized as a powerful tool for automating tasks that are complex, repetitive, or prone to human bias. It improves the efficiency, consistency and reproducibility of analyses, especially when manual methods are time-consuming or unreliable. Machine learning (ML) is a key area within this field, focusing on algorithms that can learn from data to make decisions, see Fig.1.19. This area also includes a subfield known as Deep Learning, which is based on multi-layered neural networks capable of understanding complex representations from data.

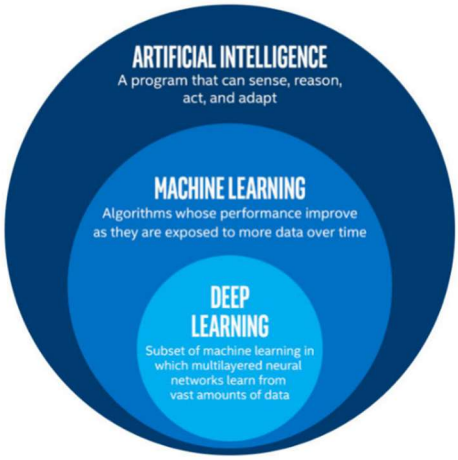

Figure 1.19. Relationship between Artificial Intelligence, Machine Learning, and Deep Learning [95]

A: Machine Learning (ML)

ML involves techniques that enable computers to learn from data without being explicitly programmed for each specific task. It helps systems recognize patterns, trends, or underlying structures in data. These patterns are then used to make predictions, classify information, or automate decision-making processes.

The main machine learning approaches are typically divided into two broad categories: supervised learning and unsupervised learning as depicted in Fig.1.20 [96].

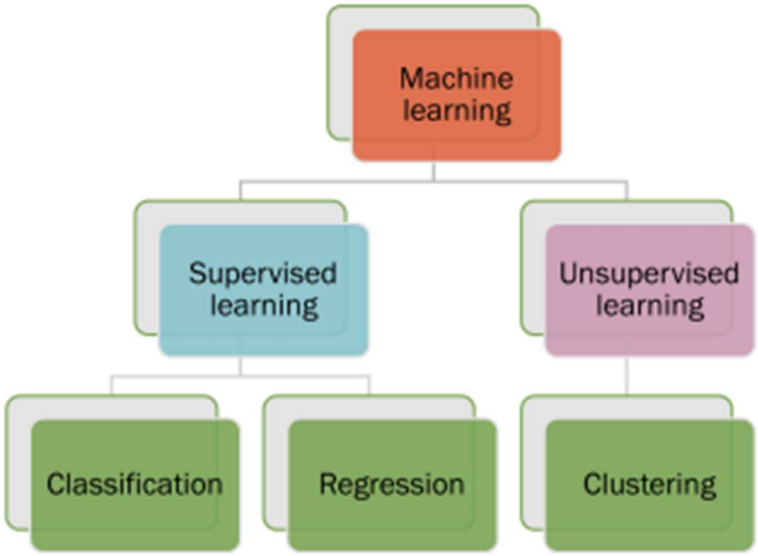

Figure 1.20. Main categories of machine learning: supervised and unsupervised learning [96]

Unsupervised learning: This approach uses algorithms designed to uncover hidden structures, clusters, or patterns within data, without requiring prior labels or annotations. It is commonly applied in clustering tasks or for dimensionality reduction [62][90][91].

Supervised learning: Unlike unsupervised learning, this method relies on labeled datasets, where each example is associated with a known output or class. From these annotated examples, the algorithm learns how to make predictions or classify new unlabeled data, enabling efficient automation of decision-making processes [62][90][91].

Many ML algorithms used for regression and classification are based on statistical learning, while others, like decision trees and SVMs, use heuristic or geometric principles. All of them aim to find patterns in data to make reliable predictions [98].

In the context of image processing, specifically for segmentation, classification, and image analysis, the typical workflow of supervised learning includes several key steps: a) image annotation, b) feature extraction, c) model training, and prediction [99], as shown in Fig.1.21.

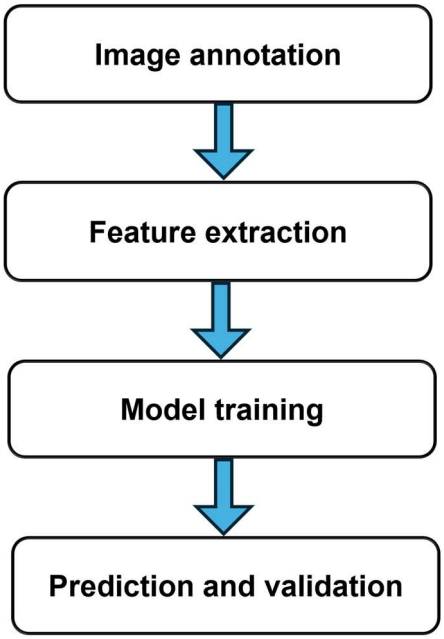

Figure 1.21. Pipeline of supervised learning in image processing

a) Image annotation

Supervised learning assumes that a system can learn generalization from a set of labeled examples. This method depends on a ground truth that is clearly defined and validated by humans, which guides the model's adjustments. However, the accuracy of the ground truth is crucial because it directly impacts the model's ability to make accurate and unbiased predictions [100].

b) Feature extraction

Feature extraction is an essential step in the workflow. It converts raw visual data into useful numerical representations. It highlights key aspects such as contrasts, textures, or gradients. These features are then used as input variables for machine learning models to help recognize or segment the structures of interest [101][68].

c) Model training

Conventional ML algorithms, such as decision trees, random forests, or support vector machines (SVMs), are trained on this labeled data. The model training goal is to learn the combinations of features that characterize each target structure [101].

d) Prediction and validation

Applying the trained model to the labeled image marks the prediction stage. During this stage, each pixel or region is classified based on the visual features that have been learned. In image analysis, this step produces an automatic segmentation of the different phases. This ensures both improved reproducibility of results and increased objectivity compared to manual methods. For thorough validation, the model is then tested on images that were not used during training to evaluate its ability to generalize [68].

B: Machine learning algorithms

In image segmentation tasks, several classical supervised classification algorithms are commonly employed. This includes Random Forest, Support Vector Machine (SVM), and k-Nearest Neighbors (k-NN). The choice of the algorithm often depends on factors such as dataset size, feature complexity, noise level and computational resources [102].

B1: Random Forest

Random Forest is an ensemble learning method that combines the output of multiple decision trees to improve the classification accuracy and reduce the risk of overfitting. In image segmentation, this approach became popular due to its ability to capture complex patterns, handle high-dimensional data and remain relatively robust to noise [103].

Each tree is trained on a bootstrap sample of the training data, meaning that each tree is trained on a randomly sampled subset of the data drawn with replacement; some examples may appear multiple times, while others may be omitted. At each split in the tree (node), a random subset of features is tested, and the best split from this subset is chosen. This approach reduces correlation among trees. At prediction time, each tree gives its own classification and the final result is given by the majority vote [104], as depicted in Fig.1.22.
Mathematically, the classification can be expressed as:

$$\boldsymbol{y(x) = mode\{h_1(x), h_2(x), \dots, h_B(x)\}} \quad \textbf{7}$$

where $h_b(x)$ stands as the prediction of b tree and $y(x)$ the final prediction of the preponderant predicted class among B trees [105].

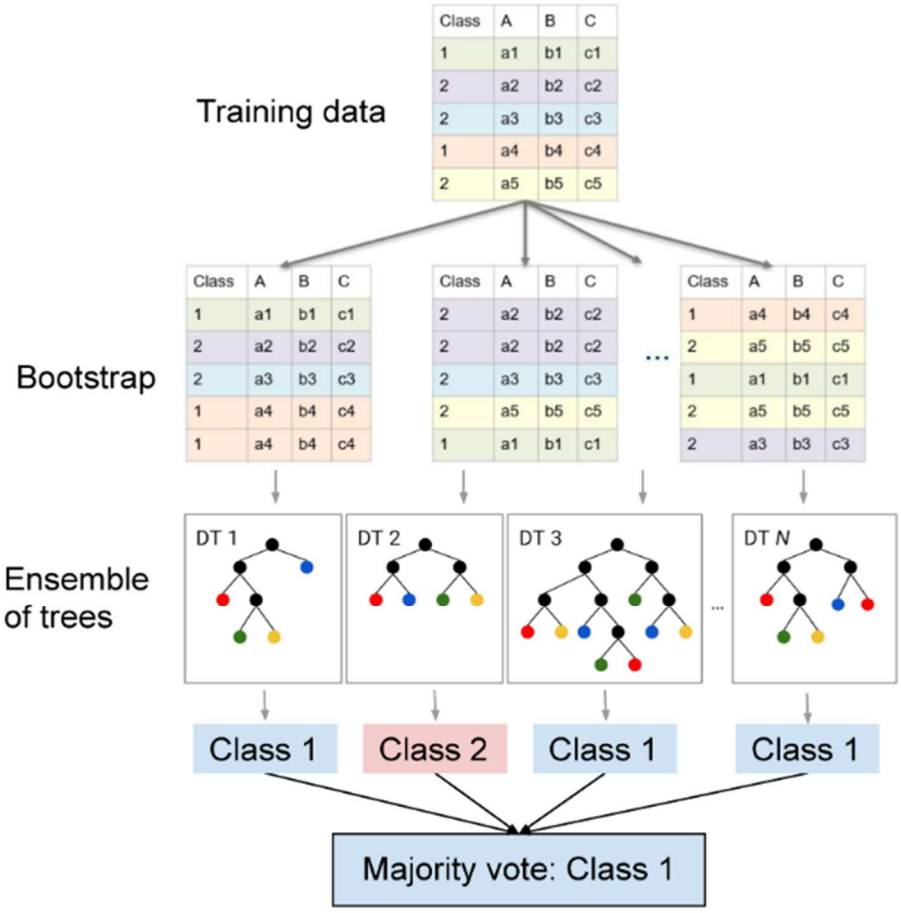

Figure 1.22. Illustration of the Random Forest ensemble learning process [106]

B2: Support Vector Machines (SVMs)

SVM aims to find the optimal hyperplane in feature space that maximizes the margin between classes [107]. The margin is defined as the distance between the hyperplane and the closest training point, called a support vector. A larger margin generally indicates better generalization to new data[108]. This principle is illustrated in Fig.1.23.

SVMs can effectively handle datasets containing many features and complex class boundaries by mapping the data into a higher-dimensional space using kernel functions. However, training an SVM can be computationally expensive on large datasets as both memory requirements and processing time may increase significantly [109][96].

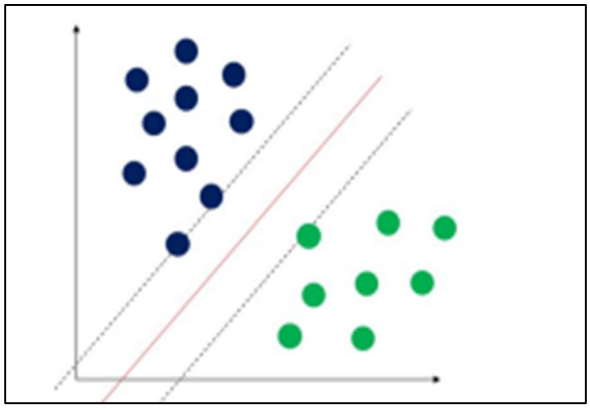

Figure 1.23. SVM illustration: the red line indicates the optimal separation between two classes; the dotted lines indicate the maximum margin and the closest points to the separation line are the support vectors [108]

B3: K-Nearest-Neighbor (k-NN)

k-NN is a simple, non-parametric classifier that assigns a class to a new data point by looking at its k nearest neighbors in the training set [110][96]. The neighbors are identified using a chosen distance metric, such as Euclidean or Manhattan distance [111].

The algorithm requires almost no training time, but classification can be shown on large datasets because the distance must be computed for all stored samples. Its accuracy is also sensitive to noise and irrelevant features [112]. Despite these limitations, k-NN can work well in multi-class problems and is often used as a baseline method [110], see Fig.1.24.

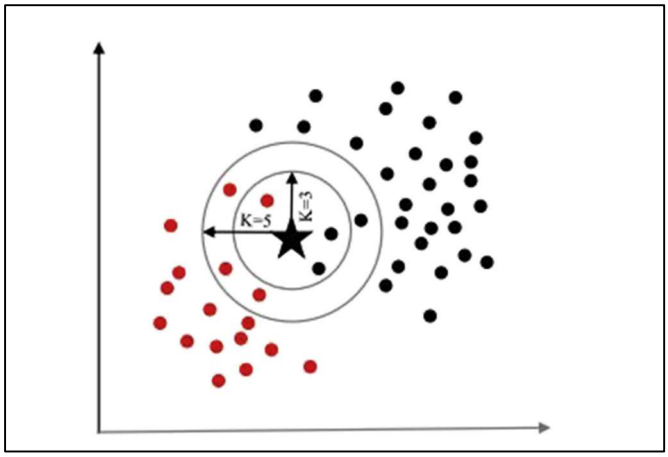

Figure 1.24. k-NN classification principle[113]

C: Deep learning: (CNNs)

Deep Learning is a subset of machine learning that utilizes deep artificial neural networks capable of automatically learning complex representations from large amounts of data. In image processing, CNNs have received significant attention. They are designed to effectively capture spatial hierarchies in images through convolutional layers. These layers learn increasingly abstract features from raw input images and pass them through the network to generate the final output.

For segmentation tasks, specialized CNN architectures such as encoder and decoder models have been developed. The encoder extracts meaningful features and the decoder upsamples these features to generate detailed pixel-wise segmentation [114].

A widely used model following this scheme is U-Net, which combines multi-scale feature extraction with precise localization to produce an accurate segmentation result [115][116]. U-Net works by combining an encoder path for feature extraction and a decoder path for resolution reconstruction, connected by skip connections that help preserve fine spatial details. Simple, fast to train, and effective even with limited data, the U-Net has become a benchmark model for segmentation tasks [117][116]. The Fig 1.25 illustrates the architecture of the U-Net model.

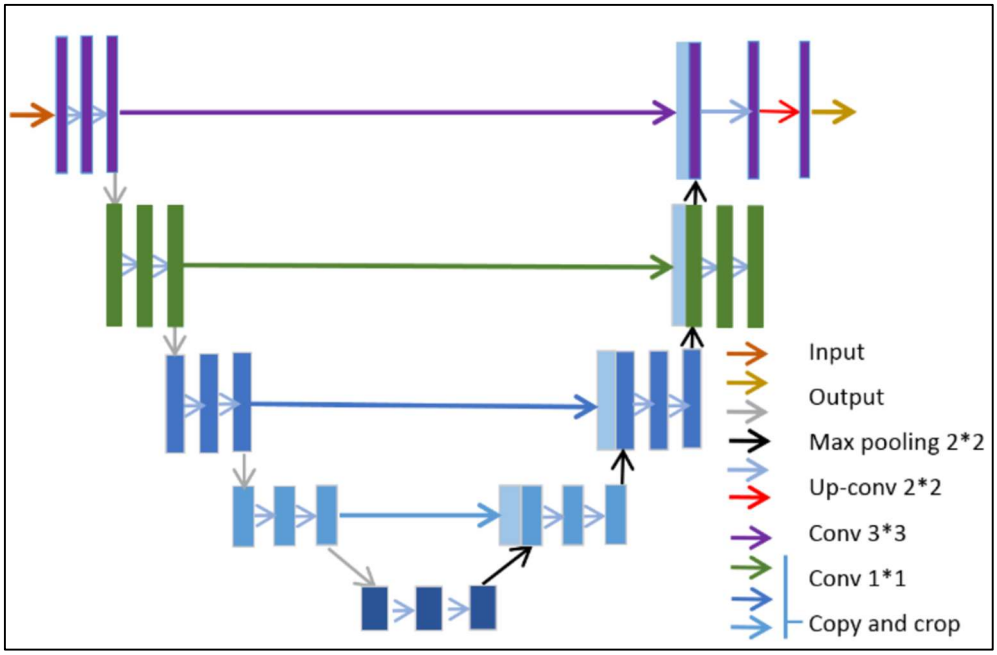

Figure 1.25. U-Net architecture [117]

PARTIAL CONCLUSION

This literature review explored key hydrogen production technologies, focusing on SOEC and PEMWE. Their structural design, operating principles and material requirements were presented together with their respective strengths and the challenges encountered during long-term operation.

Microstructural degradation phenomena, such as particle coarsening and changes in porosity, were discussed as they represent factors that can significantly reduce electrochemical performance. In this context, advanced characterization tools like FIB-SEM tomography were identified as essential for 3D visualisation and analysis of electrode architectures. In the field of image processing, traditional methods remain widely used due to their simplicity and accessibility. However, recent advances in machine learning and deep learning have brought new levels of accuracy to microstructure segmentation, although they require greater computational resources.

The insights from this review form the basis for the methodology developed in this thesis.

The next chapter will delve into the materials investigated, the imaging protocols applied and the computational tools used to implement this methodology.

CHAPTER 2:
MATERIAL AND METHODS

CHAPTER 2: MATERIAL AND METHODS

In this chapter, the tools and methods used to process the FIB-SEM data are presented. The developed methodology facilitates the transformation of raw microscopy images into meaningful numerical and visual results for detailed microstructural analysis.

2.1. Experimental part

2.1.1. Data acquisition

In this study, high-resolution FIB-SEM images (200 images) were obtained using a TESCAN AMBER X microscope (Model S8254X) at the Institute of Energy Technologies-Fundamental Electrochemistry (IET-1) of the Jülich Research Center (FZJ). Imaging occurred at around 5450× magnification, with an accelerating voltage of 20 kV and a working distance of 6 mm. The images were captured using an Everhart-Thornley (E-T) detector in high-resolution scan mode.

Each image has a spatial resolution of 50 nm per pixel in X and Y, and 100 nm in Z, a size of 95 µm in width and 65 µm in height, enabling detailed microstructural analysis. The microscope depicts a cathode region of SOEC, consisting of a porous SFM10 electrode (Layer 1), a dense Sr/Fe/O-rich deposition layer (Layer 2), a porous GDC barrier layer (Layer 3), and a dense YSZ electrolyte (Layer 4).

2.1.2. Overview of the developed image processing workflow

The automated image processing workflow for analyzing the FIB-SEM tomography datasets is organized into a series of systematic steps, as shown in Fig.2.1. This workflow combines advanced ML with traditional image processing methods.

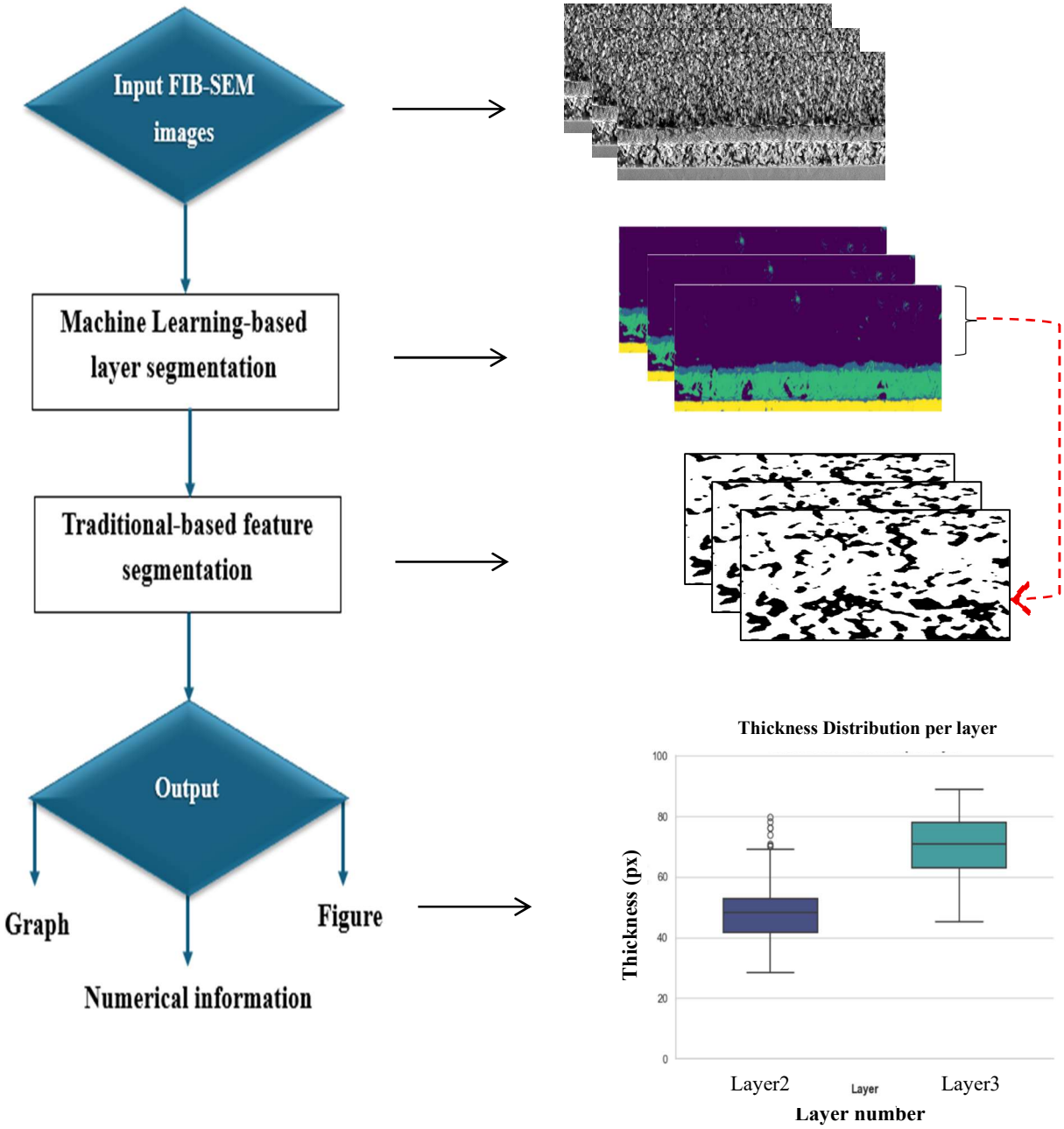

Figure 2.1. Two-Stage Image Processing workflow for FIB-SEM Images Analysis

2.1.3. Tools and overview of the data processing and analysis

The automated processing pipeline was implemented in Python 3.13.1, utilizing key libraries including OpenCV 4.11.0, Scikit-image 0.25.2, and Scikit-learn 1.7.0 for supervised machine learning with a Random Forest classifier. The approach for layer segmentation was inspired by

an example provided in Scikit-image documentation [118] (see Fig.2.2), which was adapted to the characteristics of our FIB-SEM image and the specific multi-layer structure of the SOEC electrode region.

To evaluate and calibrate the workflow, a test dataset was first prepared. A total of 200 FIB-SEM images were used. Pre-processing was first performed to correct curtaining artifacts using frequency domain filtering, then 10 representative images were manually annotated to generate training data for layer segmentation. The trained model was then used to predict the segmentation on the remaining images.

To complete the pipeline, an additional noise reduction step was applied using a median filter. Previous studies on FIB-SEM images have estimated noise by selecting homogeneous patches from each layer to minimize the influence of texture. However, due to the complexity and strong texture in our dataset, homogeneous patches were rare and potentially unrepresentative. Therefore, we opted for direct median filtering.

A traditional segmentation approach was then integrated to enable the feature extraction via multi-thresholding, allowing the quantification of morphometric parameters such as porosity and layer thickness.

Once validated, the pipeline was applied to three experimental SOECs datasets: 434 images of a pristine cell, 653 and 484 images of cells operated for 100 hours and 200 hours, respectively.

Data handling and numerical operations were supported by Numpy 2.2.6 and Pandas 2.2.3, while Matplotlib 3.10.1 and Seaborn 0.13.2 supported the visualization and statistical analysis.

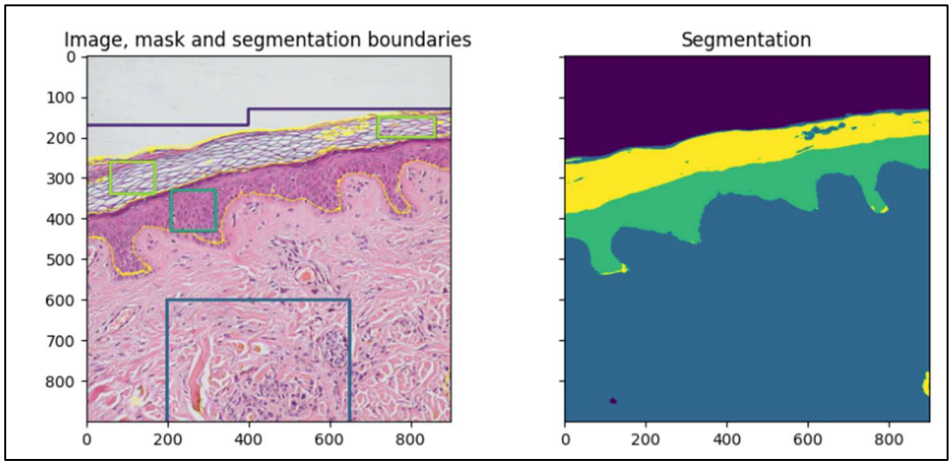

Figure 2.2. Training image: Annotated mask and predicted segmentation [118]

2.1.4. Quantitative evaluation metric

To quantitatively assess the Random Forest performance for the layer segmentation, some metrics were computed. These include global accuracy and the Jaccard index (IoU). These indicators provide complementary insights supporting the visual assessment.

- **Accuracy**

The accuracy measures the proportion of correctly classified pixels (TP + TN) relative to the total number of pixels (TP + TN + FP + FN) across the entire image.

$$\boldsymbol{Accuracy = \frac{TP + TN}{TP + TN + FP + FN}} \quad \mathbf{8}$$

Where : TP = True Positives, TN = True Negatives, FP = False Positives, FN = False Negatives

- **Jaccard index**

The Jaccard index, also known as intersection over union (IoU), measures the overlap between predicted pixels and ground-truth pixels for each layer. It provides a spatially intuitive measure of segmentation quality.

$$\boldsymbol{Jaccard\ index = \frac{|Prediction \cap GroundTruth|}{|Prediction \cup GroundTruth|}} \quad \mathbf{9}$$

The values of these metrics range from 0 to 1, where 1 indicates perfect agreement and values closer to 0 reflect poorer performance.

PARTIAL CONCLUSION

This chapter presented the experimental approach, where representative FIB-SEM images were carefully annotated to capture structural heterogeneity, providing a reliable basis for training the Random Forest classifier. Once trained, the model enables automated layer segmentation across both the test and the experimental datasets. Traditional image processing techniques were subsequently applied for noise reduction and feature segmentation.

CHAPTER 3:
RESULTS AND DISCUSSION

CHAPTER 3: RESULTS AND DISCUSSION

This chapter provides a detailed presentation of the developed pipeline and offers a comprehensive examination of the results achieved at each stage of the methodological approach.

3.1. Pipeline implementation on a single test image

To illustrate the pipeline's functioning, we first applied it to a single FIB-SEM test image. The workflow begins with ML-based segmentation, which comprises a series of steps, including preprocessing.

3.1.1 Machine Learning-based layer segmentation

This section explains in (A) the pipeline used for the segmentation (see Fig.3.1) and in (B) the quantitative evaluation metric employed to assess its performance.

A: Layer segmentation pipeline

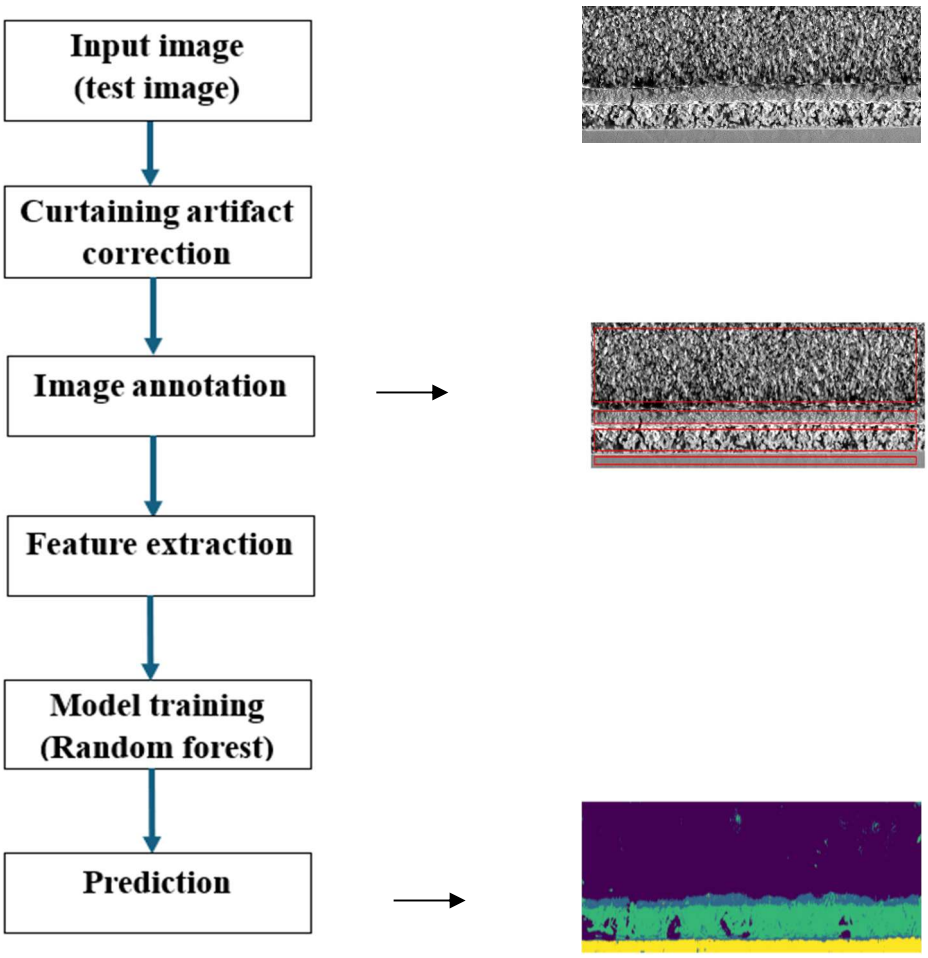

Figure 3.1. ML-based segmentation pipeline

a) Preprocessing: Curtaining artifact correction

Curtaining artifacts in FIB-SEM imaging appear as vertical or horizontal streaks caused by uneven ion milling rates during sample preparation. These periodic intensity variations can obscure fine structural details and complicate the image segmentation. To mitigate this effect, a frequency domain correction was applied. A horizontal notch filter centered at the zero vertical frequency, followed by a Hann window, was applied in the Fast Fourier Transform (FFT) domain to reduce ringing effects. Fig. 3.2 shows an example of the artifact in layer 1 and the correction after filtering. This correction notably improves image quality, contributing to more reliable segmentation outcomes.

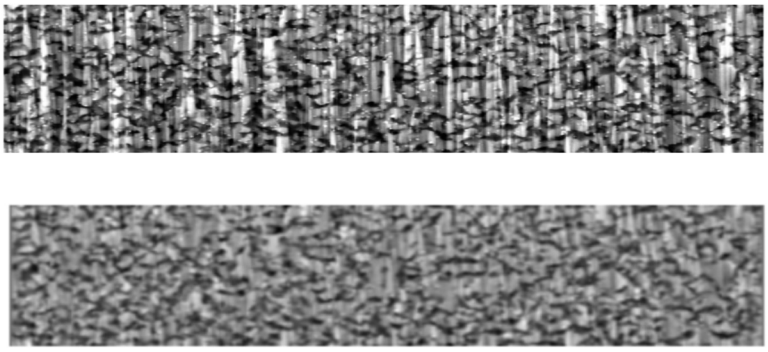

Figure 3.2. a) Unprocessed image with curtaining artifact and b) Corrected image

b) Data annotation and layer segmentation

Precise annotation forms the foundation for robust supervised machine learning. In this study, 10 representative images were manually annotated to capture the heterogeneity and challenges in layer discrimination, as depicted in Fig.3.3. The annotation was performed with attention to variations in texture, morphology, and intensity. This annotation assigns a corresponding structural class to each pixel. However, capturing the true boundary between layers 1 and 2 was challenging due to its poorly defined nature.

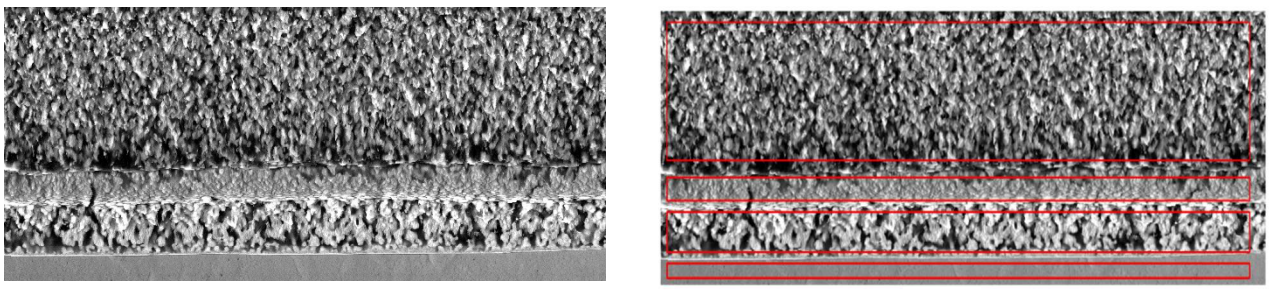

Figure 3.3. a) original image and b) manual annotation

c) Feature extraction and Random Forest training

From the annotated image, a comprehensive set of pixel-wise features was extracted using the multiscale-basic-features function from the scikit-image library. This includes: local intensity and texture at multiple spatial classes.

A Random Forest classifier, using scikit-learn, was then trained on the combined feature set. The model learns to assign each pixel to its respective layer class across the diverse annotated dataset and then makes the prediction.

The model captures approximately the overall macrostructural organisation. Especially for layer 2, the model struggles to find the right boundary. In addition, small patches of some layers appear embedded within others, likely due to overlapping intensity ranges and textural similarities. This challenge is mainly linked to the complexity of the images, see Fig.3.4.

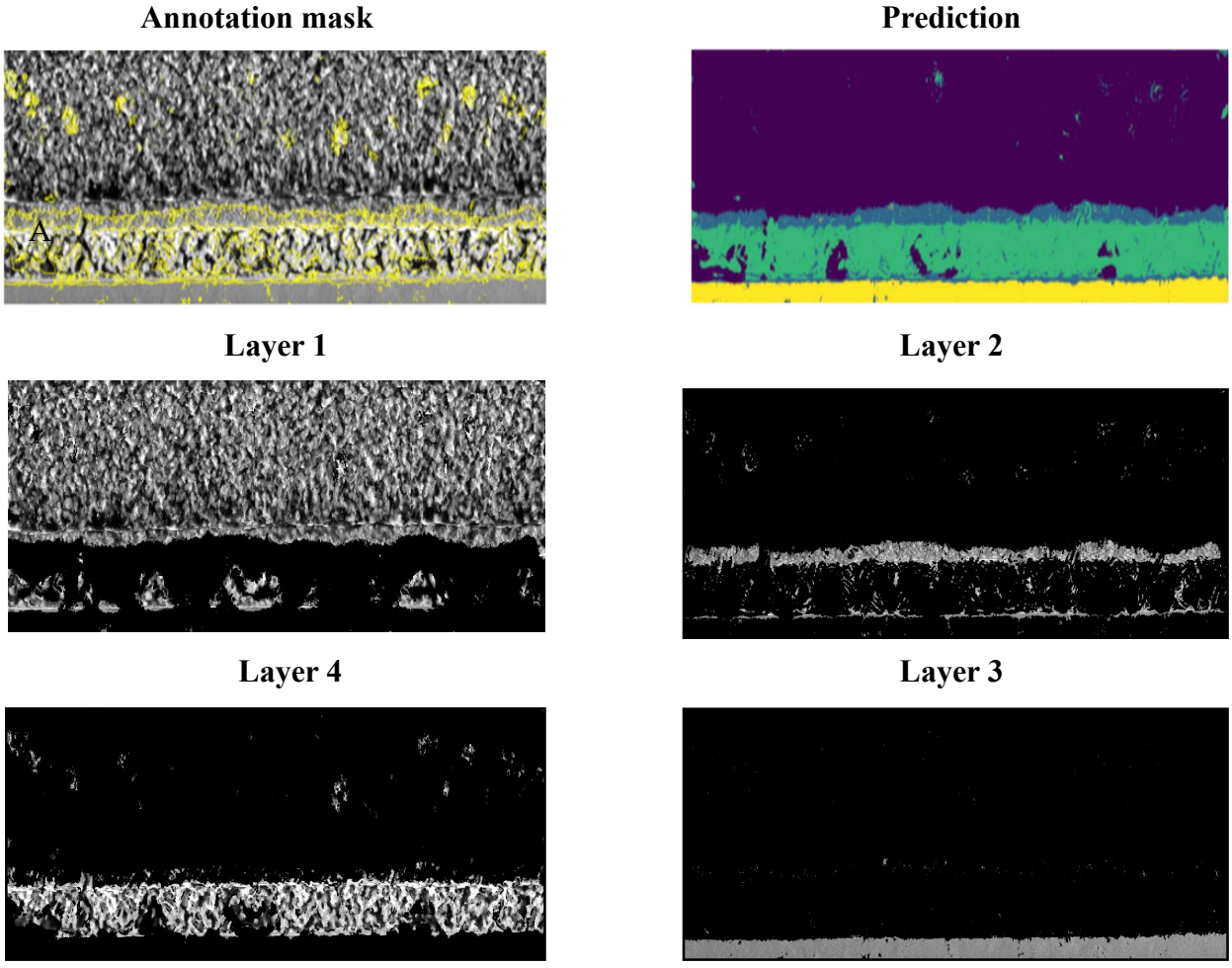

Figure 3.4. Predicted image and isolation of each layer

B: Quantitative evaluation metrics

The global accuracy and the Jaccard index (IoU) were computed. The quantitative assessment indicates an overall accuracy of 0.685, reflecting moderate effectiveness and some uncertainty in the prediction. At the layer level, layer 1 was well captured, while layer 2 continued to be the most challenging, showing a significantly lower value. Layers 3 and 4 yield intermediate results as summarized in Table 3.1.

Table 3. 1. Accuracy and Jaccard Index per layer

Metric	Global value	Layer 1	Layer 2	Layer 3	Layer 4
Accuracy	0.685				
Jaccard index		0.712	0.405	0.551	0.570

For further evaluation, the thickness of key layers was calculated column-wise by summing the pixels along the vertical axis and then averaging this value across the entire layer. Both annual measurements using GIMP, an image visualization software and automatic calculation in Python were performed. Table 3.2 summarizes the results obtained for layers 2 and 3.

Table 3. 2. Quantitative comparison of manual and automatic layer thickness

Thickness (pixels)	Tool	Layer 2	Layer 3
Manual calculation	GIMP (Measure tool)	38.2	77.58
Automatic calcualtion	Python (OpenCV script)	52.8	73.36

The automatic measurements are generally consistent with layer 3, but layer 2 shows higher values with automation. These gaps likely come from the limits of manual placement and segmentation boundaries.

Despite these setbacks, enough structural specifics or technicalities are retained by the segmentation. With the automatic approach modelled for utilization on a large volume of images, statistically investigating the datasets alleviates defects and diminishes bias.

3.1.2. Traditional-based feature segmentation

This section describes: (A) the preprocessing for noise reduction and (B) the feature segmentation using a multi-thresholding method, see Fig.3.5.

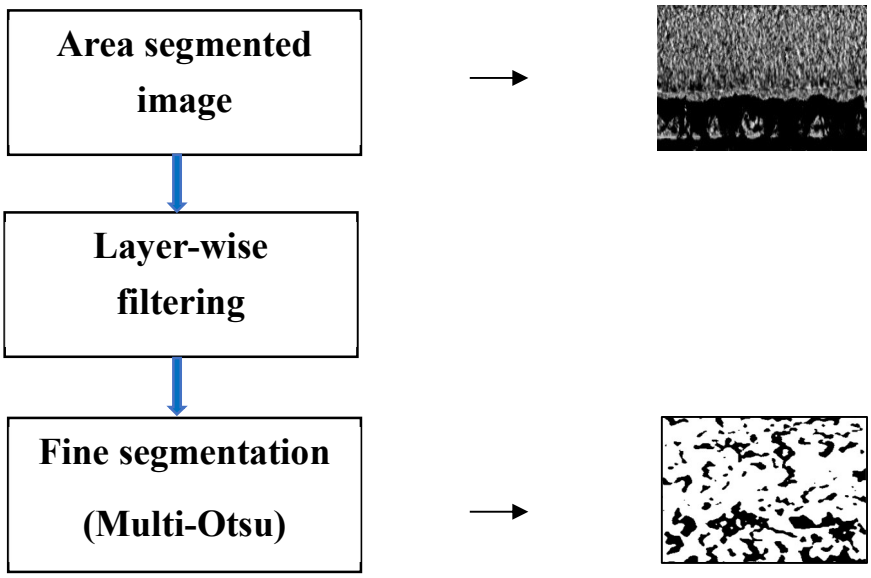

Figure 3.5. Traditional-based feature segmentation pipeline

A: Pre-processing: Noise reduction through filtering

The application of median filtering proved effective in reducing noise. This effect can be observed by comparing the original and filtered images shown in Fig.3.6. The choice of kernel size 3×3 enables control over the trade-off between noise suppression and detail preservation.

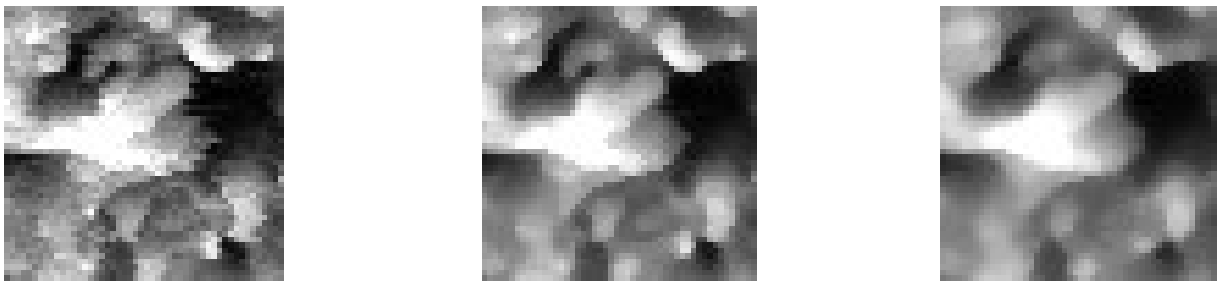

a **b** **c**

Figure 3.6. Noise reduction on 50×50 pixel patch using median filtering: a) 50×50 pixel image patch, b) Median-filtered patch using a 3×3 kernel, c) Median-filtered patch using a 5×5 kernel.

B: Multi-thresholding

A multi-thresholding approach with four thresholds dividing the image into five classes was selected. The application of Multi-Otsu thresholding effectively enhanced the separation of pores and materials, allowing clearer differentiation, as illustrated in Fig.3.8. Despite the

absence of distinct multiple bimodal peaks, this method addressed the gradual intensity heterogeneity present in the images. Fig.3.7 illustrates the basic histogram of pixel intensities and the same histogram with the threshold markers.

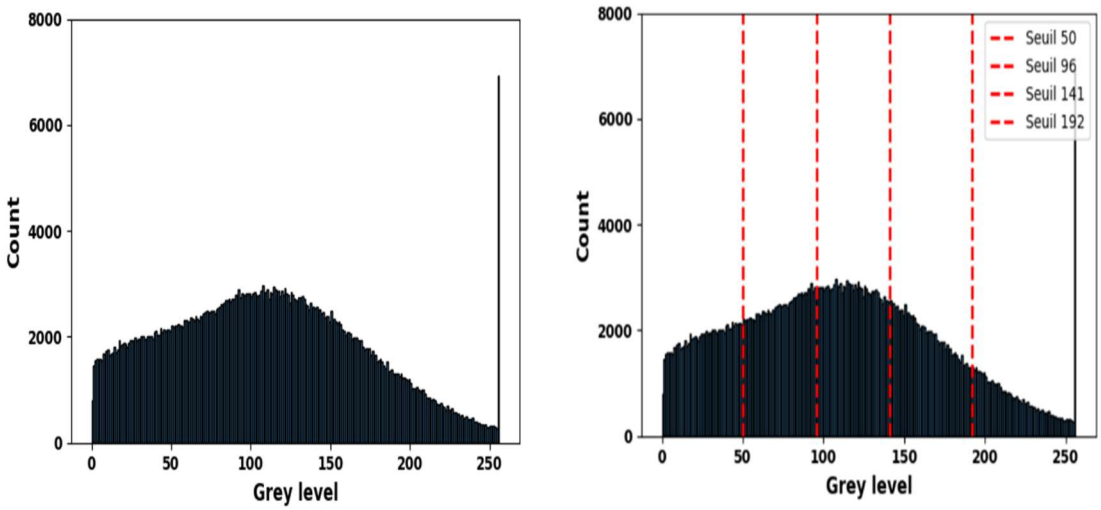

a **b**

Figure 3.7. a) pixel intensity distribution and in the first layer, b) same histogram with threshold markers

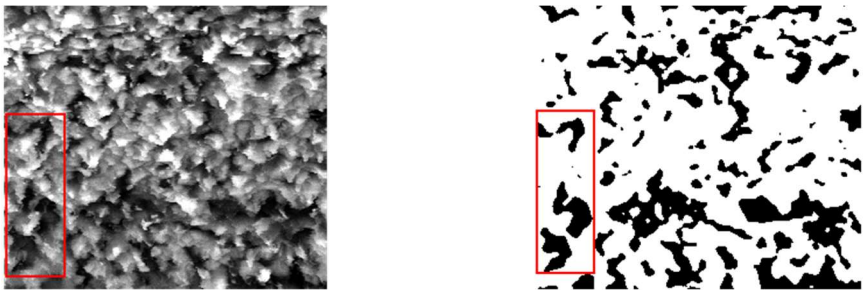

a **b**

Figure 3.8. Representation of a small region from the original image and its corresponding segmentation: a) representative area, b) segmented image

3.2. Validation of the proposed workflow on the full test dataset and real datasets

3.2.1. Validation on the full test dataset

The developed pipeline was applied to over 200 images, enabling automatic quantification of porosity and thickness. The complete workflow, combining ML-based layer segmentation,

traditional approach for porosity and thickness quantification, is summarized in Fig.3.9.

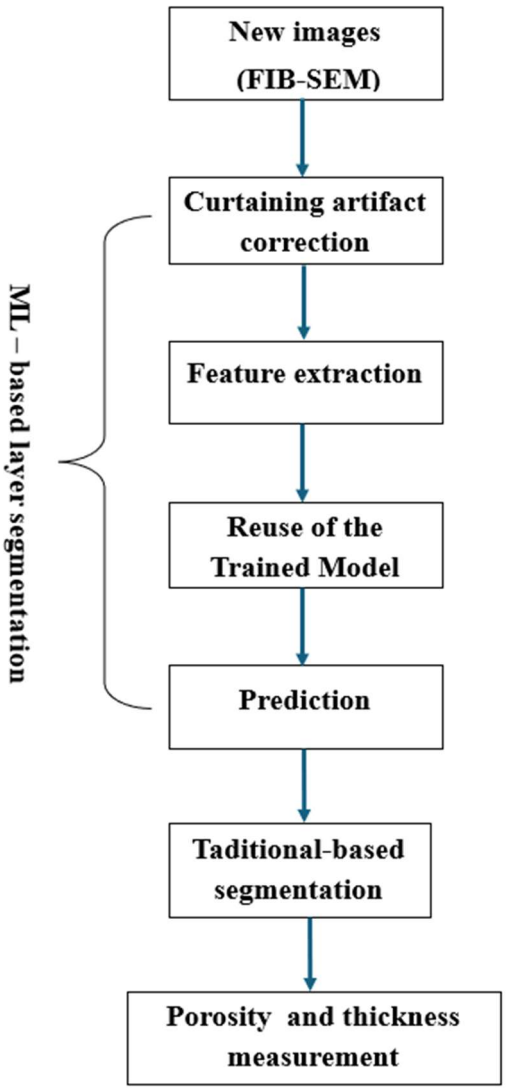

Figure 3.9. Detail workflow for FIB-SEM image analysis

For each segmented layer, the pore area was calculated as the percentage of pixels classified as pores relative to the total area of the layer.

Fig.3.10 illustrates respectively the porosity distribution for layers and the thickness measurement for layers 2 and 3.

Layer 1 shows the highest porosity (20%), which can be justified by the presence of more open areas compared with the other layers. Layer 2, initially a dense layer, reveals almost no detectable porosity, whereas layer 3 is moderately porous (14%).

In terms of thickness, layer 2 averages around (45px) compared to layer 3, (70px). This is consistent with what can be visually observed in the original images.

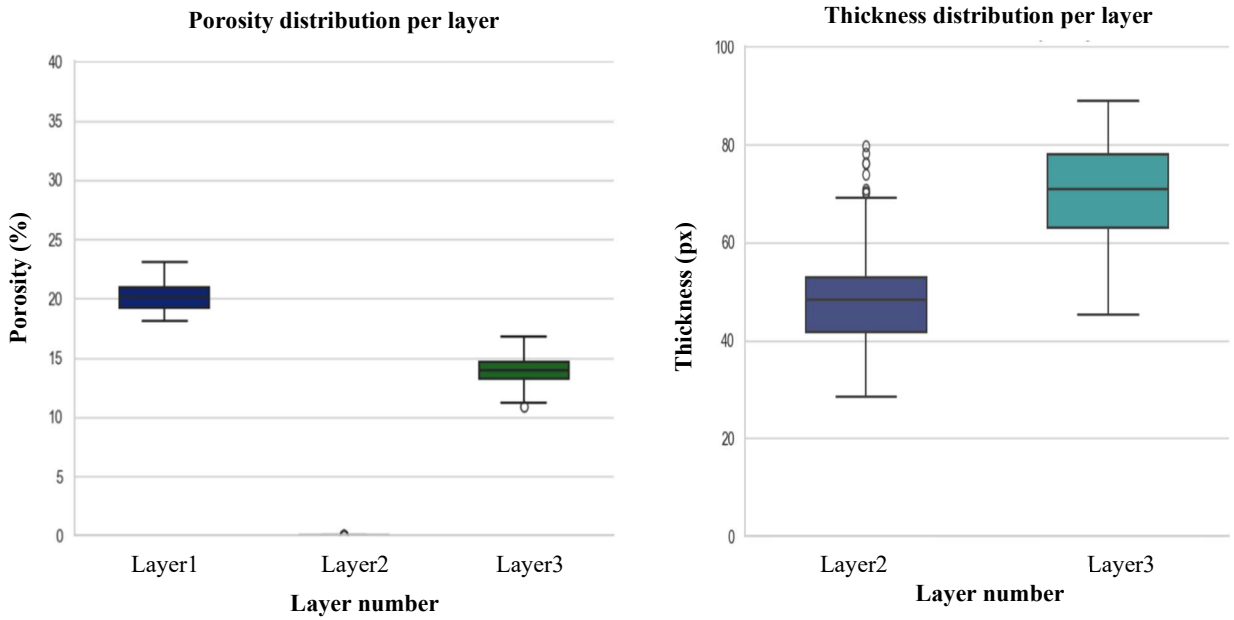

Figure 3.10. Porosity and thickness distribution across the test dataset

3.2.2. Validation on real datasets

The same segmentation pipeline, from layer segmentation to feature segmentation, was reused for the three additional SOEC datasets: pristine cell, a 100-hour run cell, and a 200-hour run cell. For each dataset, representative images were manually annotated and the model was trained and used for prediction following the same protocol, see Fig.3.11.

a) Original b) Label mask c) Predicted

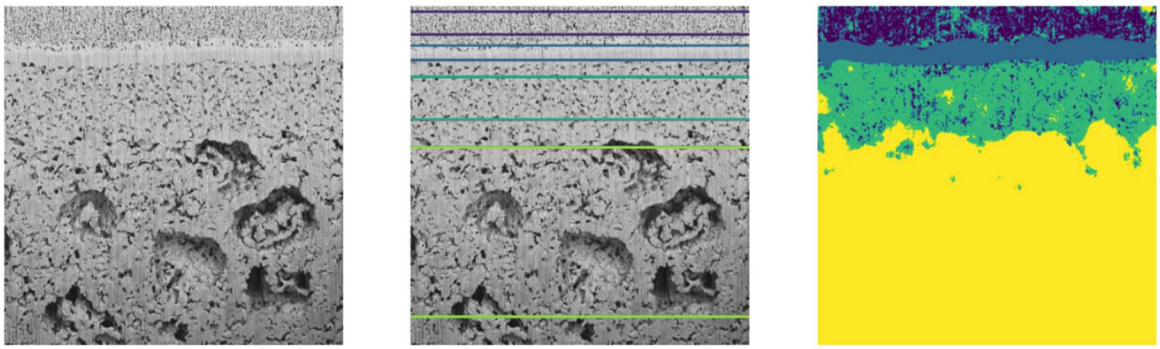

Figure 3.11. Pristine sample: a) original micrograph, b) ground truth mask and c) segmented image

a) Porosity

The comparative analysis reveals that layer 4 exhibits a clear upward trend in porosity across the datasets. In contrast, the other layers display a similar trend but with more irregularities, as shown in Fig. 3.12. This inconsistency may be attributed to segmentation errors between certain layers. It may also be attributed to the fact that pores in these regions are relatively small

compared to the overall image resolution, leading to potential measurement errors.

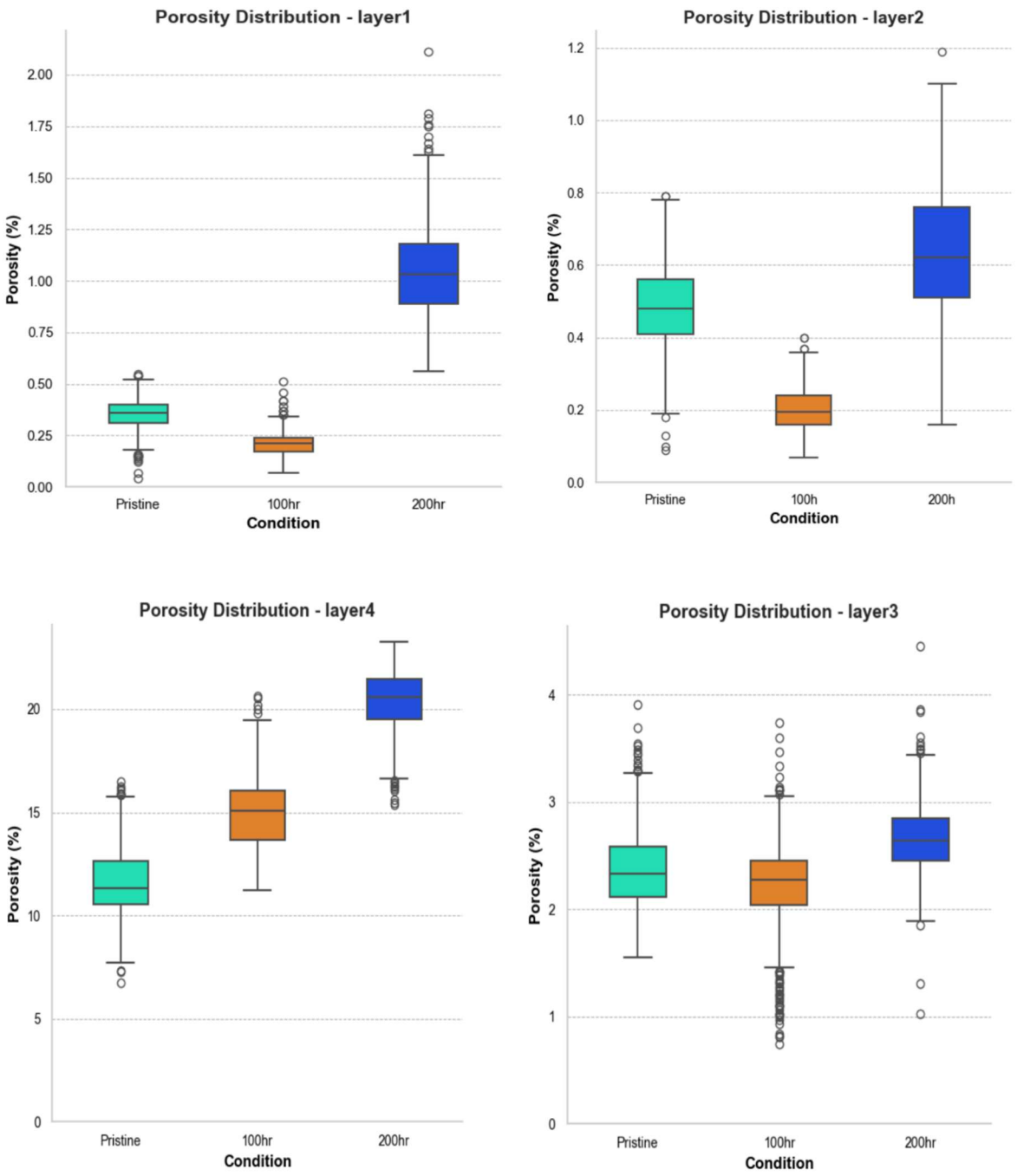

Figure 3.12. Porosity distribution across layers under different cycle conditions

b) Thickness

Among the layers analyzed, layer 2 demonstrates more consistent and accurate segmentation across all datasets, providing a reliable basis for thickness comparison. For layer 2, the median

thickness is approximately 100 px in the pristine state, increases slightly to about 110 px after 100 hours, then increases substantially to roughly 150 px after 200 hours, see Fig.3.13

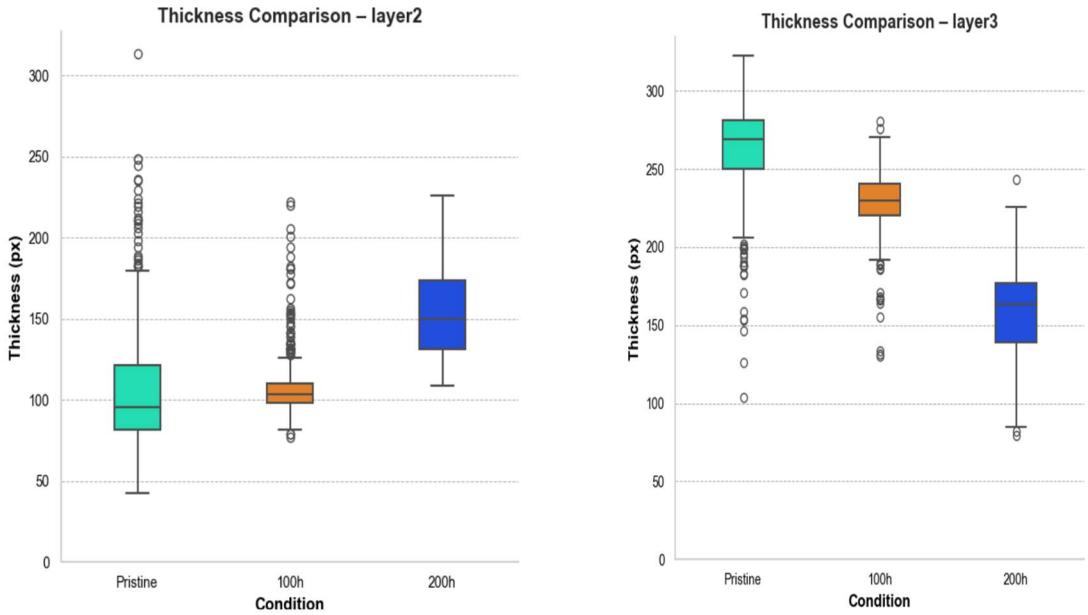

Figure 3.13. Thickness distribution across layer 2 and layer 3 under different cycle conditions

The overall trend reveals a significant evolution in thickness over operational time, indicating the presence of material degradation or transformation processes in this layer. The layers that show a consistent trend can be considered as a reliable indicator of material changes due to aging. Conversely, layers with irregular trends highlight areas where segmentation accuracy may need improvement.

PARTIAL CONCLUSION

The combined pipeline, using Random Forest for layer segmentation and thresholding for feature segmentation, was applied to multilayer FIB-SEM images. For layer partitioning, the model achieved a moderate accuracy of 0.68 with varying Jaccard indices across layers. Its application to pristine, 100-hour, and 200-hour SOEC-operated samples revealed consistent trends. Layer 4 showed a clear increase in porosity, whereas layers 1 and 3 exhibited similar but less regular porosity trends, likely due to segmentation challenges and small pore sizes relative to image resolution. Thickness analysis was focused on layer 2, which was well segmented across datasets.

GENERAL CONCLUSION AND PERSPECTIVES

GENERAL CONCLUSION AND PERSPECTIVES

Image processing plays a central role in the quantitative analysis of microstructures. In the case of FIB-SEM images, the challenge lies in the high complexity of the data, requiring carefully designed methods to extract meaningful information. While deep learning methods have proved excellent in many cases, their computational cost and implementation complexity often limit their accessibility.

This study shows the practical feasibility of automating the analysis of multilayer FIB-SEM images of the SOEC electrode catalyst part by utilizing traditional approaches and supervised machine learning. Based on computational efficiency, our workflow improves the accessibility of microstructural quantification in this research domain.

The methodology involved labeling a representative dataset, training a Random Forest classifier to automatically identify the electrode layers and implementing a traditional segmentation approach to isolate porous regions. On the test set, the layer segmentation achieved an accuracy of 68%. Despite this moderate outcome, the application of the entire developed pipeline on the large datasets allows us to identify meaningful trends in the microstructure. Its extension on real experimental datasets enabled monitoring the evolution of porosity and thickness with aging in some layers. Specifically, layer 4 exhibited a clear increase in porosity during aging, while layer 2 was consistently well segmented across the datasets, from the pristine state to 100h and 200h of operation. These observations are consistent with some expected physical degradation mechanisms. However, a deeper investigation by a material scientist would be required to fully interpret the underlying causes and the implications of these trends. In addition, the average processing time for examining 483 images was approximately 9 minutes. This emphasizes the pipeline's practicality for regular utilization in research environments.

Due to potential challenges in image resolution and segmentation errors, inconsistencies were identified in some layers across different datasets. Thus, improvements are needed. Future work should focus on refining the annotation protocol to enhance the reliability of labels. It should also explore advanced features to help the model better distinguish labels. Finally, methods combining machine learning and deep learning could be tested as long as computational efficiency and ease use are taken into account.

REFERENCES

[1] B. Z. Eneviratne, S.I., X. Zhang, M. Adnan, W. Badi, C. Dereczynski, A. Di Luca, S. Ghosh, I. Iskandar, J. Kossin, S. Lewis, F. Otto, I. Pinto, M. Satoh, S.M. Vicente-Serrano, M. Wehner, "Weather and Climate Extreme Events in a Changing Climate," 2023. doi: 10.1017/9781009157896.013.

[2] IPCC, "Foreword Technical and Preface," 2019.

[3] International Energy Agency, "Assessing the Effects of Economic Recoveries on Global Energy Demand adn CO2 Emissions in 2021," 2021.

[4] E. Commission, "Communication from the commission to the council and the European parliament," 2019.

[5] International Energy Agency (IEA), "Global Hydrogen Review 2024 - Transport by pipeline," pp. 113–124, 2024, [Online]. Available: www.iea.org

[6] A. Di Nardo, M. Portarapillo, D. Russo, and A. Di Benedetto, "Hydrogen production via steam reforming of different fuels: thermodynamic comparison," *Int. J. Hydrogen Energy*, vol. 55, no. July 2023, pp. 1143–1160, 2024, doi: 10.1016/j.ijhydene.2023.11.215.

[7] I. Staffell, D.Scamman, A.Velazquez, P.Balcombe, P.Dodds, P.Ekins, N. Shah , "The role of hydrogen and fuel cells in the global energy system," *Energy Environ. Sci.*, vol. 12, no. 2, pp. 463–491, 2019, doi: 10.1039/c8ee01157e.

[8] A. Franco and C. Giovannini, "Recent and Future Advances in Water Electrolysis for Green Hydrogen Generation: Critical Analysis and Perspectives," *Sustain.*, vol. 15, no. 24, 2023, doi: 10.3390/su152416917.

[9] L. Espina-Romero, H. Gutiérrez Hurtado, D. Ríos Parra, R. A. Vilchez Pirela, R. Talavera-Aguirre, and A. Ochoa-Díaz, "Challenges and Opportunities in the Implementation of AI in Manufacturing: A Bibliometric Analysis," *Sci*, vol. 6, no. 4, 2024, doi: 10.3390/sci6040060.

[10] M. Bonanno, K. Muller, B.Bensmann, R.Hanke-Rauschenbach, D. Aili, T. Franken, A. Chromik, R. Peach, A. Freiberg, S.Thiele, "Review and Prospects of PEM Water Electrolysis at Elevated Temperature Operation," *Adv. Mater. Technol.*, vol. 9, no. 2, pp. 1–25, 2024, doi: 10.1002/admt.202300281.

[11] Y. Chi, Li. P, Z. Zexin, Z. Yu, R. Qi, S. Mu, Y. Song, J. Lin, "Active balance of a solid oxide electrolysis cell stack tower: Circuit design and control strategy," *Appl. Energy*, vol. 399, no. March, p. 126432, 2025, doi: 10.1016/j.apenergy.2025.126432.

[12] S. E. Wolf, F.E. Winterhalder, V.Vibhu, L. G. J. de Haart, O. Guillon, R. A. Eichel, N. H. Menzler., "Solid oxide electrolysis cells - current material development and industrial application," *J. Mater. Chem. A*, vol. 11, no. 34, pp. 17977–18028, 2023, doi: 10.1039/d3ta02161k.

[13] C. M. Ruse, L. A. Hume, Y. Wang, T. C. Pesacreta, and X. D. Zhou, "Quantifying Microstructure Features for High-Performance Solid Oxide Cells," *Materials (Basel).*, vol. 17, no. 11, pp. 1–21, 2024, doi: 10.3390/ma17112622.

[14] X. Ma and Y. Yu, "Training Tricks for Steel Microstructure Segmentation with Deep Learning," *Processes*, vol. 11, no. 12, 2023, doi: 10.3390/pr11123298.

[15] K. S. Tan, C. K. Lam, W. C. Tan, H. S. Ooi, and Z. H. Lim, "A review of image processing and quantification analysis for solid oxide fuel cell," *Energy AI*, vol. 16, no. February, p. 100354, 2024, doi: 10.1016/j.egyai.2024.100354.

[16] J. P. Stempien, *Fundamental Aspects of Solid Oxide Electrolyzer Cell Modelling and the Application for the System Level Analysis*, no. October 2014. doi: 10.13140/RG.2.1.2746.2006.

[17] J. Weissbart and R. Ruka, "A Solid Electrolyte Fuel Cell," *J. Electrochem. Soc.*, vol. 109, no. 8, p. 723, 1962, doi: 10.1149/1.2425537.

[18] H. S. Spacil and C. S. Tedmon, "Electrochemical Dissociation of Water Vapor in Solid Oxide Electrolyte Cells," *J. Electrochem. Soc.*, vol. 116, no. 12, p. 1627, 1969, doi: 10.1149/1.2411643.

[19] G. Schiller, A. Ansar, M. Lang, and O. Patz, "High temperature water electrolysis using metal supported solid oxide electrolyser cells (SOEC)," *J. Appl. Electrochem.*, vol. 39, no. 2, pp. 293–301, 2009, doi: 10.1007/s10800-008-9672-6.

[20] K. Chen, N. Ai, and S. P. Jiang, "Development of (Gd,Ce)O[sub 2]-Impregnated (La,Sr)MnO[sub 3] Anodes of High Temperature Solid Oxide Electrolysis Cells," *J. Electrochem. Soc.*, vol. 157, no. 11, p. P89, 2010, doi: 10.1149/1.3481436.

[21] S. Chen, K. Xie, D. Dong, H. Li, Q. Qin, Y. Zhang, Y. Wu, "A composite cathode based on scandium-doped chromate for direct high-temperature steam electrolysis in a symmetric solid oxide electrolyzer," *J. Power Sources*, vol. 274, pp. 718–729, 2015, doi: 10.1016/j.jpowsour.2014.10.103.

[22] A. Hauch, R. Küngas, P. Blennow, A. B. Hansen, J. B. Hansen, J. B, B.V Mathiesen, M. B. Mogensen, "Recent advances in solid oxide cell technology for electrolysis," *Science (80-.).*, vol. 370, no. 6513, 2020, doi: 10.1126/science.aba6118.

[23] J. Davies, F. Dolci, and E. Weidner, "Historical Analysis of FCH 2 JU Electrolyser Projects Evaluation of contributions towards advancing the State of the Art," 2021. doi: 10.2760/951902.

[24] M. A. Laguna-Bercero, "Recent advances in high temperature electrolysis using solid oxide fuel cells: A review," *J. Power Sources*, vol. 203, pp. 4–16, 2012, doi: 10.1016/j.jpowsour.2011.12.019.

[25] G. Flis and G. Wakim, "Solid Oxide Electrolysis: A Technology Status Assessment," *Clean Air Task Force*, no. November. 2023.

[26] L. A. Jolaoso, I. T. Bello, O. A. Ojelade, A. Yousuf, C. Duan, and P. Kazempoor, "Operational and scaling-up barriers of SOEC and mitigation strategies to boost H2 production- a comprehensive review," *Int. J. Hydrogen Energy*, vol. 48, no. 85, pp. 33017–33041, 2023, doi: 10.1016/j.ijhydene.2023.05.077.

[27] A. Pandiyan, A. Uthayakumar, R. Subrayan, S. W. Cha, and S. B. K. Moorthy, "Review of solid oxide electrolysis cells: A clean energy strategy for hydrogen generation," *Nanomater. Energy*, vol. 8, no. 1, 2019, doi: 10.1680/jnaen.18.00009.

[28] Z. Geng, F. Wei-Cheng, S. Yue-Feng, and W. Guo-Xiong, "Recent Advances in Anode Materials of Solid Oxide Electrolysis Cells," *J. Electrochem.*, vol. 29, no. 2, 2023, doi: 10.13208/j.electrochem.2215006.

[29] S. He, Y. Zou, K. Chen, and S. P. Jiang, “A critical review of key materials and issues in solid oxide cells,” *Interdiscip. Mater.*, vol. 2, no. 1, pp. 111–136, 2023, doi: 10.1002/idm2.12068.

[30] Y. Sun, D. Jin, X. Zhang, Q. Shao, C. Guan, R. Li, F. Cheng, X. Lin, G. Xiao, J. Wang, “Controllable Technology for Thermal Expansion Coefficient of Commercial Materials for Solid Oxide Electrolytic Cells,” *Materials (Basel).*, vol. 17, no. 5, 2024, doi: 10.3390/ma17051216.

[31] E. Drożdż-Cieśla, J. Wyrwa, J. Broś, and M. Rękas, “Structural, microstructural, thermal, and electrical properties of Ni/YSZ cermet materials,” *J. Therm. Anal. Calorim.*, vol. 108, no. 3, pp. 1051–1057, 2012, doi: 10.1007/s10973-012-2281-y.

[32] M. Mori, T. Yamamoto, H. Itoh, H. Inaba, and H. Tagawa, “Thermal Expansion of Nickel-Zirconia Anodes in Solid Oxide Fuel Cells during Fabrication and Operation,” *J. Electrochem. Soc.*, vol. 145, no. 4, pp. 1374–1381, 1998, doi: 10.1149/1.1838468.

[33] K. Haberko, M. Jasinski, P. Pasierb, M. Radecka, and M. Rekas, “Structural and electrical properties of Ni-YSZ cermet materials,” *J. Power Sources*, vol. 195, no. 17, pp. 5527–5533, 2010, doi: 10.1016/j.jpowsour.2010.03.050.

[34] K. Sato, S. Watanabe, Y. Huang, T. Miyasaka, T. Matsui, K. Yashiro, T. Kawada, K. Amezawa, K. Kumada, K. Eguchi, “Relationship between microstructure and deformation of porous Ni-based cermets under redox cycling,” *SN Appl. Sci.*, vol. 3, no. 10, 2021, doi: 10.1007/s42452-021-04789-w.

[35] M. Dai, F. Li, S. Fang, D. He, J. Lu, Y. Zhang, X. Cao, J. Liu, D. Chen, Y. Chen, Y. Luo, “Advances in Nanostructured Electrodes for Solid Oxide Cells by Infiltration or Exsolution,” *Materials (Basel).*, vol. 18, no. 8, pp. 1–37, 2025, doi: 10.3390/ma18081802.

[36] W. Yang, Z. Pan, Z. Jiao, Z. Zhong, and R. O’Hayre, “Advanced microstructure characterization and microstructural evolution of porous cermet electrodes in solid oxide cells: a comprehensive review,” *Energy Rev.*, vol. 4, no. 1, p. 100104, 2024, doi: 10.1016/j.enrev.2024.100104.

[37] S. Guo, L. Jiang, Y. Li, P. Zhong, A. S. Ismail, T. Norby, D. Han, “From Electrolyte and Electrode Materials to Large-Area Protonic Ceramic Fuel Cells: A Review,” *Adv. Funct. Mater.*, vol. 34, no. 32, 2024, doi: 10.1002/adfm.202304729.

[38] S. P. S. Badwal, F. T. Ciacchi, and D. Milosevic, “Scandia-zirconia electrolytes for intermediate temperature solid oxide fuel cell operation,” *Solid State Ionics*, vol. 136–137, pp. 91–99, 2000, doi: 10.1016/S0167-2738(00)00356-8.

[39] J. Jiang, W. Shen, and J. L. Hertz, “Structure and ionic conductivity of nanoscale gadolinia-doped ceria thin films,” *Solid State Ionics*, vol. 249–250, pp. 139–143, 2013, doi: 10.1016/j.ssi.2013.08.003.

[40] M. Zhang, E. Wang, J. Mao, H. Wang, M. Ouyang, and H. Hu, “Performance analysis of a metal-supported intermediate-temperature solid oxide electrolysis cell,” *Front. Energy Res.*, vol. 10, no. September, pp. 1–18, 2022, doi: 10.3389/fenrg.2022.888787.

[41] “PEM Fuel Cells.” Accessed: Jul. 02, 2025. [Online]. Available: https://americanhistory.si.edu/fuelcells/pem/pemmain.htm?

[42] G. G. Gagliardi, A. Ibrahim, D. Borello, and A. El-Kharouf, “Composite polymers development and application for polymer electrolyte membrane technologies-a review,” *Molecules*, vol. 25, no. 7, 2020, doi: 10.3390/molecules25071712.

[43] L. J. N. and A. P. F. J. H. Russell, “1. 5 1. 5,” in *Most*, 1973, pp. 13–15.

[44] X. Li, Y. Yao, Y. Tian, J. Jia, W. Ma, X. Yan, J. Liang, “Recent advances in key components of proton exchange membrane water electrolysers,” *Mater. Chem. Front.*, vol. 8, no. 13, pp. 2493–2510, 2024, doi: 10.1039/d4qm00086b.

[45] M. Carmo, D. L. Fritz, J. Mergel, and D. Stolten, “A comprehensive review on PEM water electrolysis,” *Int. J. Hydrogen Energy*, vol. 38, no. 12, pp. 4901–4934, 2013, doi: 10.1016/j.ijhydene.2013.01.151.

[46] C. R. Wang, J. M. Stansberry, R. Mukundan, H. M. J. Chang, D. Kulkarni, A. M. Park, A. B. Plymill, N. M. Firas, P. C. Liu, J. T. Lang, J. K. Lee, N. E. Tolouei, Y. Morimoto, C. Wang, G. Zhu, J. Brouwer, P. Atanassor, C. B. Capuano, C. Mittelstealdt, X. Peng, I. V. Zenyuk, “Proton Exchange Membrane Water Electrolysis: Cell-Level Considerations for Gigawatt-Scale Deployment,” *Chem. Rev.*, 2025, doi: 10.1021/acs.chemrev.3c00904.

[47] B. Endrődi, C. A. Trapp, I. Szén, I. Bakos, M. Lukovics, and C. Janáky, “Challenges and Opportunities of the Dynamic Operation of PEM Water Electrolyzers,” *Energies*, vol. 18, no. 9, pp. 1–11, 2025, doi: 10.3390/en18092154.

[48] S. Wang, A. Lu, and C. J. Zhong, “Hydrogen production from water electrolysis: role of catalysts,” *Nano Converg.*, vol. 8, no. 1, 2021, doi: 10.1186/s40580-021-00254-x.

[49] S. Shiva Kumar and V. Himabindu, “Hydrogen production by PEM water electrolysis – A review,” *Mater. Sci. Energy Technol.*, vol. 2, no. 3, pp. 442–454, 2019, doi: 10.1016/j.mset.2019.03.002.

[50] F. Hegge, R. Moroni, P. Trinke. B. Bensmann, R. Hanke-Raushenbach, S. Thiele, S. Vierrath, “Three-dimensional microstructure analysis of a polymer electrolyte membrane water electrolyzer anode,” *J. Power Sources*, vol. 393, no. January, pp. 62–66, 2018, doi: 10.1016/j.jpowsour.2018.04.089.

[51] E. Zagoraiou, S. Krishan, A. Siriwardana, A. M. Moschovi, and I. Yakoumis, “Performance of Stainless-Steel Bipolar Plates (SS-BPPs) in Polymer Electrolyte Membrane Water Electrolyser (PEMWE): A Comprehensive Review,” *Compounds*, vol. 4, no. 2, pp. 252–267, 2024, doi: 10.3390/compounds4020013.

[52] N. Sezer, S. Bayhan, U. Fesli, and A. Sanfilippo, “A comprehensive review of the state-of-the-art of proton exchange membrane water electrolysis,” *Mater. Sci. Energy Technol.*, vol. 8, no. January 2024, pp. 44–65, 2025, doi: 10.1016/j.mset.2024.07.006.

[53] S. Yuan, C. Zhao, L. Luo, C. Fu, H. Li, Lu. An, X. Cheng, S. Shen, J. Yin. X. Yan, J. Zhang, “Revealing the Role of the Ionomer at the Triple-Phase Boundary in a Proton-Exchange Membrane Water Electrolyzer,” *J. Phys. Chem. Lett.*, vol. 15, no. 19, pp. 5223–5230, 2024, doi: 10.1021/acs.jpclett.4c00851.

[54] H. Li, S. Yuan, J. You, C. Zhao, X. Cheng, L. Luo, X. Yan, S. Shen, J. Zhang , “Revealing the Oxygen Transport Challenges in Catalyst Layers in Proton Exchange Membrane Fuel Cells and Water Electrolysis,” *Nano-Micro Lett.*, vol. 17, no. 1, pp. 1–46, 2025, doi: 10.1007/s40820-025-01719-y.

[55] T. Wang, X. Cao, and L. Jiao, “PEM water electrolysis for hydrogen production:

fundamentals, advances, and prospects," *Carbon Neutrality*, vol. 1, no. 1, pp. 1–19, 2022, doi: 10.1007/s43979-022-00022-8.

[56] "L'électrolyse PEM (Proton Exchange Membrane)," Discover the greentech. Accessed: Aug. 02, 2025. [Online]. Available: https://www.discoverthegreentech.com/hydrogene/production/electrolyse/electrolyse-pem/

[57] C. Klose, T. Saatkamp, A. Münchinger, L. Bohn, G. Titvinidze, M.Breitwieser, K. D. Kreuer, S. Vierrath, "All-Hydrocarbon MEA for PEM Water Electrolysis Combining Low Hydrogen Crossover and High Efficiency," *Adv. Energy Mater.*, vol. 10, no. 14, pp. 1–9, 2020, doi: 10.1002/aenm.201903995.

[58] X. Sun, S. C. Simonsen, T. Norby, and A. Chatzitakis, "Composite membranes for high temperature PEM fuel cells and electrolysers: A critical review," *Membranes (Basel).*, vol. 9, no. 7, 2019, doi: 10.3390/membranes9070083.

[59] X. Luo, G. Lau, M. Tesfaye, C. R. Arthurs, I. Cordova, C. Wang, M. Yandrasits, A. Kusoglu, "Thickness Dependence of Proton-Exchange-Membrane Properties," *J. Electrochem. Soc.*, vol. 168, no. 10, p. 104517, 2021, doi: 10.1149/1945-7111/ac2973.

[60] K. Chen and S. P. Jiang, "Review—Materials Degradation of Solid Oxide Electrolysis Cells," *J. Electrochem. Soc.*, vol. 163, no. 11, pp. F3070–F3083, 2016, doi: 10.1149/2.0101611jes.

[61] M. Ananyev, A. Gavrilyuk, D. Bronin, R. Steinberger-Wilckens, and J. Mertens, "SOFC degradation quantification using image analysis," *Eur. Fuel Cell Forum 2011*, no. June, pp. B0421–B0434, 2011.

[62] S. De Angelis, P. S. Jørgensen, V. Esposito, E. H. R. Tsai, M. Holler, K. Kreka, E. Abdellahi, J. R. Bowen, "Ex-situ tracking solid oxide cell electrode microstructural evolution in a redox cycle by high resolution ptychographic nanotomography," *J. Power Sources*, vol. 360, pp. 520–527, 2017, doi: 10.1016/j.jpowsour.2017.06.035.

[63] P. Marmet, L. Holzer, T. Hocker, G. K. Boiger, H. Bausinger, A. Mai, M. Fingerle, S. Reeb, D. Michel, J. M. Brader., "Standardized microstructure characterization of SOC electrodes as a key element for Digital Materials Design," *Energy Adv.*, vol. 2, no. 7, pp. 980–1013, 2023, doi: 10.1039/d3ya00132f.

[64] T. Rodenas and G. Prieto, "FIB-SEM tomography in catalysis and electrochemistry," *Catal. Today*, vol. 405–406, no. April, pp. 2–13, 2022, doi: 10.1016/j.cattod.2022.09.013.

[65] M. Kishimoto, H. Iwai, M. Saito, and H. Yoshida, "Quantitative evaluation of solid oxide fuel cell porous anode microstructure based on focused ion beam and scanning electron microscope technique and prediction of anode overpotentials," *J. Power Sources*, vol. 196, no. 10, pp. 4555–4563, 2011, doi: 10.1016/j.jpowsour.2010.12.100.

[66] J. Becher, T. L. Sheppard, Y. Fam, S. Baier, W. Wang, S. Kulkarni, T. E. Keller, M. Lyubomirskiy, D. Brueckner, M. Kahnt, A. Schropp, C. G. Schroer, J. D. Grunwaldt, "Mapping the Pore Architecture of Structured Catalyst Monoliths from Nanometer to Centimeter Scale with Electron and X-ray Tomographies," *J. Phys. Chem. C*, vol. 123, no. 41, pp. 25197–25208, 2019, doi: 10.1021/acs.jpcc.9b06541.

[67] J. Joos, B. Rüger, T. Carraro, A. Weber, and E. Ivers-Tiffée, "Electrode Reconstruction

by FIB/SEM and Microstructure Modeling," *ECS Trans.*, vol. 28, no. 11, pp. 81–91, 2010, doi: 10.1149/1.3495834.

[68] M. H. Mobarak, M. A. Mimona, A. M. Islam, N. Hossain, T. F. Zohura, I. Imtiaz, M. I. H. Rimon, "Scope of machine learning in materials research—A review," *Appl. Surf. Sci. Adv.*, vol. 18, no. August, p. 100523, 2023, doi: 10.1016/j.apsadv.2023.100523.

[69] N. Otsu, "A Threshold Selection Method from Gray-Level Histograms," *IEEE Trans. Syst. Man Cybern.*, vol. 9, no. 1, pp. 62–66, 1979.

[70] L. C. Chen, G. Papandreou, I. Kokkinos, K. Murphy, and A. L. Yuille, "DeepLab: Semantic Image Segmentation with Deep Convolutional Nets, Atrous Convolution, and Fully Connected CRFs," *IEEE Trans. Pattern Anal. Mach. Intell.*, vol. 40, no. 4, pp. 834–848, 2018, doi: 10.1109/TPAMI.2017.2699184.

[71] N. Tajbakhsh, L. Jeyaseelan, Q. Li, J. N. Chiang, Z. Wu, and X. Ding, "Embracing imperfect datasets: A review of deep learning solutions for medical image segmentation," *Med. Image Anal.*, vol. 63, p. 101693, 2020, doi: 10.1016/j.media.2020.101693.

[72] H. Hwang, J. Ahn, H. Lee, J. Oh, J. Kim, J. P. Ahn, H. K. Kim, J. H. Lee, Y. Yoon, J. H. Hwang, "Deep learning-assisted microstructural analysis of Ni/YSZ anode composites for solid oxide fuel cells," *Mater. Charact.*, vol. 172, no. October 2020, 2021, doi: 10.1016/j.matchar.2021.110906.

[73] S. M. Bae, Y. H. Kim, Y. H. You, and J. H. Hwang, "Extraction of quantitative parameters for describing the microstructure of solid oxide fuel cells," *Microsc. Microanal.*, vol. 19, no. SUPPL. 5, pp. 140–144, 2013, doi: 10.1017/S1431927613012518.

[74] A. Sotiras, C. Davatzikos, and N. Paragios, "Deformable medical image registration: A survey," *IEEE Trans. Med. Imaging*, vol. 32, no. 7, pp. 1153–1190, 2013, doi: 10.1109/TMI.2013.2265603.

[75] V.Mazet, "Denoising," github. Accessed: Aug. 13, 2025. [Online]. Available: https://vincmazet.github.io/bip/restoration/denoising.html

[76] Cloudinary, "Image Contrast Enhancement," accessed: Aug. 13, 2025. [Online]. Available: https://cloudinary.com/glossary/image-contrast-enhancement

[77] N. Rossberg, S. Corrie, and L. Grøndahl, "Automated analysis of pore structures in biomaterials," 2025, doi: 10.1039/d5tb00848d.

[78] Cloudinary, "Region Growing," accessed: Aug. 13, 2025. [Online]. Available: https://cloudinary.com/glossary/region-growing

[79] The MathWorks, "Types of Morphological Operations," accessed: Aug. 13, 2025. [Online]. Available: https://fr.mathworks.com/help/images/morphological-dilation-and-erosion.html

[80] B. Zitová and J. Flusser, "Image registration methods: A survey," *Image Vis. Comput.*, vol. 21, no. 11, pp. 977–1000, 2003, doi: 10.1016/S0262-8856(03)00137-9.

[81] V. González-Ruiz, M. R. Fernández-Fernández, and J. J. Fernández, "Structure-preserving Gaussian denoising of FIB-SEM volumes," *Ultramicroscopy*, vol. 246, no. December 2022, pp. 0–10, 2023, doi: 10.1016/j.ultramic.2022.113674.

[82] A. W. and E. W. R. Fisher, S.Perkins, “Gaussian Smoothing.” Accessed: Aug. 05, 2025. [Online]. Available: https://homepages.inf.ed.ac.uk/rbf/HIPR2/gsmooth.htm??

[83] FunVision Tutorials, “Opencv C++ tutorial : Smoothing, blur, noise reduction / canceling,” accessed: Aug. 21, 2025. [Online]. Available: https://www.funvisiontutorials.com/2020/04/opencv-c-tutorial-smoothing-blur-noise.html

[84] S. Guan, B. Liu, S. Chen, Y. Wu, F. Wang, X. Liu, R. Wei, “Adaptive median filter salt and pepper noise suppression approach for common path coherent dispersion spectrometer,” *Sci. Rep.*, vol. 14, no. 1, pp. 1–18, 2024, doi: 10.1038/s41598-024-66649-y.

[85] Ghhennam, “Traitements de Lissage Filtrage Du Bruits.” Accessed: Aug. 05, 2025. [Online]. Available: https://www.scribd.com/document/498672542/Chapitre-3-Traitements-de-Lissage-Filtrage-Du-Bruits

[86] Y. Jiang, H. Wang, Y. Cai, and B. Fu, “Salt and Pepper Noise Removal Method Based on the Edge-Adaptive Total Variation Model,” *Frontiers (Boulder).*, vol. 8, no. June, pp. 1–9, 2022, doi: 10.3389/fams.. 2022.918357.

[87] P. Härtinger and C. Steger, “Adaptive histogram equalization in constant time,” *J. Real-Time Image Process.*, vol. 21, no. 3, pp. 1–9, 2024, doi: 10.1007/s11554-024-01465-1.

[88] S. Kansal, S. Purwar, and R. K. Tripathi, “Image contrast enhancement using unsharp masking and histogram equalization,” *Multimed. Tools Appl.*, vol. 77, no. 20, pp. 26919–26938, 2018, doi: 10.1007/s11042-018-5894-8.

[89] M. Xu, S. Chen, X. Gao, Q. Ye, Y. Ke, C. Huo, X. Liu, “Research on Fast Multi-Threshold Image Segmentation Technique Using Histogram Analysis,” *Electron.*, vol. 12, no. 21, 2023, doi: 10.3390/electronics12214446.

[90] X. Yang, X. Shen, J. Long, and H. Chen, “An Improved Median-based Otsu Image Thresholding Algorithm,” *AASRI Procedia*, vol. 3, pp. 468–473, 2012, doi: 10.1016/j.aasri.2012.11.074.

[91] V. Mazet, “Histogram thresholding,” github. Accessed: Aug. 13, 2025. [Online]. Available: https://vincmazet.github.io/bip/segmentation/histogram.html

[92] “Multi-Otsu Thresholding.” Accessed: Aug. 05, 2025. [Online]. Available: https://scikit-image.org/docs/0.25.x/auto_examples/segmentation/plot_multiotsu.html

[93] H. M. Zangana, A. K. Mohammed, and F. Mahmood Mustafa, “Advancements in Edge Detection Techniques for Image Enhancement: A Comprehensive Review,” *Int. J. Artif. Intell. Robot.*, vol. 6, no. 1, pp. 29–39, 2024, doi: 10.25139/ijair.v6i1.8217.

[94] K. S. Tan, C. K. Lam, W. C. Tan, H. S. Ooi, and Z. H. Lim, “A review of image processing and quantification analysis for solid oxide fuel cell,” *Energy AI*, vol. 16, no. December 2023, p. 100354, 2024, doi: 10.1016/j.egyai.2024.100354.

[95] B. Prüfer, D.-I. Olaf Zukunft Zweitgutachter, and Z. Ru Dai, *Machine Learning Image Processing: Techniques and Applications*. 2024.

[96] Q. An, S. Rahman, J. Zhou, and J. J. Kang, “A Comprehensive Review on Machine Learning in Healthcare Industry: Classification, Restrictions, Opportunities and Challenges,” *Sensors*, vol. 23, no. 9, 2023, doi: 10.3390/s23094178.

[97] G. Ciaburro, G. Iannace, M. Ali, A. Alabdulkarem, and A. Nuhait, “An artificial neural network approach to modelling absorbent asphalts acoustic properties,” *J. King Saud Univ. - Eng. Sci.*, vol. 33, no. 4, pp. 213–220, 2021, doi: 10.1016/j.jksues.2020.07.002.

[98] C. M. Bishop, *Pattern Recognition and Machine Learning*. 2006.

[99] Vihar Kurama, “Machine Learning Image Processing: Techniques and Applications,” Nanonets. Accessed: Aug. 05, 2025. [Online]. Available: https://nanonets.com/blog/machine-learning-image-processing/

[100] V. Taran, Y. Gordienko, A. Rokovyi, O. Alienin, and S. Stirenko, *Impact of Ground Truth Annotation Quality on Performance of Semantic Image Segmentation of Traffic Conditions*, vol. 938. Springer International Publishing, 2020. doi: 10.1007/978-3-030-16621-2_17.

[101] S. Gudadhe, A. Thakare, and A. M. Anter, “A novel machine learning-based feature extraction method for classifying intracranial hemorrhage computed tomography images,” *Healthc. Anal.*, vol. 3, no. April, p. 100196, 2023, doi: 10.1016/j.health.2023.100196.

[102] P. Thanh Noi and M. Kappas, “Comparison of Random Forest, k-Nearest Neighbor, and Support Vector Machine Classifiers for Land Cover Classification Using Sentinel-2 Imagery,” *Sensors (Basel).*, vol. 18, no. 1, 2017, doi: 10.3390/s18010018.

[103] T. Merkulova and B. Jayakumar, “Evaluation framework for Image Segmentation Algorithms,” 2025, [Online]. Available: http://arxiv.org/abs/2504.04435

[104] C. Bouvier, N. Souedet, J. Levy, C. Jan. Z. You, A. S. Herard, G. Mergoil, B. H. Rodriguez, C. Clouchoux, T. Delzescaux, “Reduced and stable feature sets selection with random forest for neurons segmentation in histological images of macaque brain,” *Sci. Rep.*, vol. 11, no. 1, pp. 1–17, 2021, doi: 10.1038/s41598-021-02344-6.

[105] R. Khanduri, “Master thesis Fraud detection in Credit Cards using Machine Learning technologies,” 2020.

[106] “Image classification - Random Forests,” Humboldt-Universität zu Berlin. Accessed: Aug. 10, 2025. [Online]. Available: https://eol.pages.cms.hu-berlin.de/geo_rs/S08_Image_classification2.html

[107] A. Grønlund, L. Kamma, and K. G. Larsen, “Near-tight margin-based generalization bounds for support vector machines,” *37th Int. Conf. Mach. Learn. ICML 2020*, vol. PartF16814, pp. 3737–3746, 2020.

[108] B. A.-E. Aiad, K. B. Zarif, Z. M. Gadallah, and H. A. EL-kareem, “Support Vector Machine Kernel Functions Comparison,” *Int. Undergrad. Res. Conf.*, vol. 5, no. 5, pp. 84–88, 2021.

[109] “Why does the training process become computationally expensive for large datasets?,” EITCA. Accessed: Aug. 13, 2025. [Online]. Available: https://eitca.org/artificial-intelligence/eitc-ai-mlp-machine-learning-with-python/support-vector-machine/svm-training/examination-review-svm-training/why-does-the-training-process-become-computationally-expensive-for-large-datasets/

[110] R. K. Halder, M. N. Uddin, M. A. Uddin, S. Aryal, and A. Khraisat, “Enhancing K-nearest neighbor algorithm: a comprehensive review and performance analysis of modifications,” *J. Big Data*, vol. 11, no. 1, 2024, doi: 10.1186/s40537-024-00973-y.

[111] Wikipedia,“k-nearest neighbors algorithm,” [Online]. Available: https://en.wikipedia.org/wiki/K-nearest_neighbors_algorithm

[112] “K-Nearest Neighbours Explained, Practical Guide & How To Tutorial In Python,” SPOT INTELLIGENCE. Accessed: Aug. 13, 2025. [Online]. Available: https://spotintelligence.com/2023/08/22/k-nearest-neighbours/

[113] P. Dutta, S. Paul, and A. Kumar, “Comparative analysis of various supervised machine learning techniques for diagnosis of COVID-19.”

[114] A. Kouidri, “Understanding DeepLabV3 in Image Segmentation,” Ikomia. Accessed: Aug. 10, 2025. [Online]. Available: https://www.ikomia.ai/blog/understanding-deeplabv3-image-segmentation

[115] Y. Lecun, Y. Bengio, and G. Hinton, “Deep learning,” *Nature*, vol. 521, no. 7553, pp. 436–444, 2015, doi: 10.1038/nature14539.

[116] N. Navab, J. Hornegger, W. M. Wells, A. F. Frangi, and D. Hutchison, *Medical Image Computing and Computer-Assisted Intervention – MICCAI*. 2015.

[117] Y. Ding, F. Chen, Y. Zhao, Z. Wu, C. Zhang, and D. Wu, “A Stacked Multi-Connection Simple Reducing Net for Brain Tumor Segmentation,” *IEEE Access*, vol. 7, pp. 104011–104024, 2019, doi: 10.1109/ACCESS.2019.2926448.

[118] Scikit-image,“Trainable segmentation using local features and random forests.” Accessed: Aug. 19, 2025. [Online]. Available: https://scikit-image.org/docs/0.24.x/auto_examples/segmentation/plot_trainable_segmentation.html

APPENDIX

```
# Libraries
import cv2
import numpy as np
import os
from tqdm import tqdm
import pandas as pd
import seaborn as sns
import matplotlib.pyplot as plt
from skimage.io import imread, imsave
from skimage import feature, segmentation
from skimage.future import predict_segmenter, fit_segmenter
from sklearn.ensemble import RandomForestClassifier
from functools import partial
from skimage.filters import threshold_multiotsu
from skimage.util import img_as_ubyte
from skimage.color import gray2rgb, rgb2gray

############################################################

# --- Mask creation ---

def create_mask(image, layers):
    """Create a mask for one image slice based on layer coordinates"""
    mask = np.zeros_like(image, dtype=np.uint8)
    for idx, (y_range, x_range) in enumerate(layers, start=1):
        y_min, y_max = y_range
        x_min, x_max = x_range
        mask[y_min:y_max, x_min:x_max] = idx
    return mask

# --- Preprocessing ---
def fft_filter(img, mask_h=2, mask_gap=5):
    """Removes curtaining artifacts on FIB/SEM images using FFT filtering"""

    img_h, img_w = img.shape
    fft_img = np.fft.fftshift(np.fft.fft2(img))
    # Mask horizontal frequencies in the Fourier domain
```

```
    fft_img[int(img_h/2)-mask_h:int(img_h/2)+mask_h, 0:int(img_w/2-img_w*mask_gap/2/100)] = 0
    fft_img[int(img_h/2)-mask_h:int(img_h/2)+mask_h,   int(img_w/2+img_w*mask_gap/2/100):img_w]
= 0
    real_img = np.fft.ifftn(np.fft.ifftshift(fft_img)).real
    real_img = real_img + np.abs(np.min(real_img))
    real_img = real_img / np.max(real_img)
    real_img = img_as_ubyte(real_img)
    return real_img

# --- Feature extraction ---
def extract_features(image, sigma_min=1, sigma_max=16):
    """Extract multiscale features for machine learning-based segmentation"""

    features_func = partial(
        feature.multiscale_basic_features,
        intensity=True,
        edges=False,
        texture=True,
        sigma_min=sigma_min,
        sigma_max=sigma_max,
        channel_axis=None)
    return features_func(image)

# --- Model training ---
def training_model(image, mask, sigma_min=1, sigma_max=16):
    """Train Random Forest model on a single image and its mask"""

    image_filt = fft_filter(image)
    feats = extract_features(image_filt, sigma_min, sigma_max)
    model = RandomForestClassifier(n_estimators=100, max_depth=100, max_samples=0.05, n_jobs=-
1)
    model = fit_segmenter(mask, feats, model)
    print("Model training complete.")

# --- Visualization ---
    fig, axes = plt.subplots(1, 3, figsize=(15, 5), sharex=True, sharey=True)

    axes[0].imshow(image_filt, cmap='gray')
    axes[0].axis('off')
```

```
    axes[0].set_title('Original image')
    axes[1].imshow(segmentation.mark_boundaries(image_filt, mask, mode='thick'))
    axes[1].contour(mask)
    axes[1].axis('off')
    axes[1].set_title('Label mask')
    axes[2].imshow(predict_segmenter(feats, model))
    axes[2].axis('off')
    axes[2].set_title('Predicted result')

    plt.tight_layout()
    plt.show()

    return model

# --- prediction ---
def predict_segmentation(image, model):
    image = fft_filter(image)
    features = extract_features(image)
    predicted_mask = predict_segmenter(features, model)
    return predicted_mask

# --- Visualization ---
def visualize_prediction(image, predicted_mask):
    """Display original image with predicted segmentation"""
    fig, axes = plt.subplots(1, 2, figsize=(12, 5), sharex=True, sharey=True)
    axes[0].imshow(segmentation.mark_boundaries(image, predicted_mask, mode='thick'))
    axes[0].set_title('Segmentation Boundaries')
    axes[0].axis('off')
    axes[1].imshow(predicted_mask, cmap='viridis')
    axes[1].set_title('Predicted Segmentation')
    axes[1].axis('off')

    plt.tight_layout()
    plt.show()



### Porosity and thickness calculation functions
```

```
# --- Common function for Porosity calculation ---

def process_layer(model, max_layer, fixed_thresholds, idx_range,
                  save_csv_path="results.csv"):
    porosity_list = []
    thickness_list = []
    y_indices = []

    for y in tqdm(idx_range):
        #test_img = stack[:, y, :]
        test_img = load_image(y)
        result = predict_segmentation(test_img, model)

        cur_porosity=[]
        cur_thickness=[]

        for label_layer in range(max_layer):
            label_layer = label_layer+1 #label_layer = [1,2,3,...]
            mask_layer = (result==label_layer)

            # Isolate layer of interest (label_layer)
            layer_img = test_img.copy()
            layer_img[result != label_layer] = 255

            # Median filter
            median_filtered = cv2.medianBlur(layer_img, 5)

            # Multi-otsu thresholding for segmentation
            layer_binary = np.digitize(median_filtered, bins=fixed_thresholds)

            # Binary mask (0 for "pore")
            mask_binary = np.ones_like(layer_binary) * 255
            mask_binary[layer_binary == 0] = 0

            area_layer = np.sum(mask_layer)
            area_pores = np.sum(mask_binary == 0)
            porosity = round((area_pores / area_layer) * 100, 2) if area_layer > 0 else 0
            cur_porosity.append(porosity)
```

```
            ##################################################

            # Thickness per column (sum along vertical axis=0)

            thickness_per_column = np.sum(mask_layer, axis=0)

            # Mean thickness for the slice, rounded to 2 decimals
            average_thickness = np.round(np.mean(thickness_per_column), 2)

            cur_thickness.append(average_thickness)

        porosity_list.append(cur_porosity)
        thickness_list.append(cur_thickness)
        y_indices.append(y)

    # Save porosity
    layer_num1 = []
    for i in range(max_layer): layer_num1.append('layer'+str(i+1)+' [%]')
    df1 = pd.DataFrame(porosity_list, index=y_indices, columns=layer_num1)

    df1.to_csv(save_csv_path[:-4]+'_porosity.csv', index=False)
    print(f"Porosity saved")
    print(df1.describe())

    #### save thickness
    layer_num2 = []
    for j in range(max_layer): layer_num2.append('layer'+str(j+1)+' [px]')
    df2 = pd.DataFrame(thickness_list, index=y_indices, columns=layer_num2)

    df2.to_csv(save_csv_path[:-4]+'_thickness.csv', index=False)
    print(f"thickness saved")
    print(df2.describe())

    return df1, df2

Plotting functions
#### Porosity

def plot_porosity_comparison(csv_paths, *layer_names, ylim=None):
```

```
"""
Plot porosity distribution comparison for multiple layers from a single CSV file.
"""

all_data = []
for path in csv_paths:
    df = pd.read_csv(path)
    for layer_name in layer_names:
        if layer_name not in df.columns:
            raise ValueError(f"'{layer_name}' not found in {path}")

    # Melt data to long format for seaborn
    df_melted = pd.melt(df[list(layer_names)])

    # Rename columns for seaborn
    df_melted.columns = ['Layer', 'Porosity (%)']

    all_data.append(df_melted)

df_long = pd.concat(all_data, ignore_index=True)

# Remove '[%]' suffix for cleaner x-axis labels
df_long['Layer'] = df_long['Layer'].str.replace(r'\s*\[%\]', '', regex=True)

sns.set(style="whitegrid")
plt.figure(figsize=(6, 6))

palette = ['#03fcc2', '#ff7f0e', '#033dfc']

ax = sns.boxplot(
    x='Layer',
    y='Porosity (%)',
    data=df_long,
    palette=palette,
    width=0.5,
    linewidth=1.5
)

ax.set_xlabel("Layer", fontsize=12, fontweight='bold')
```

```
ax.set_ylabel("Porosity [%]", fontsize=12, fontweight='bold')

ax.tick_params(axis='x', colors='black', width=0.8)
for label in ax.get_xticklabels():
    label.set_fontweight('normal')
    label.set_color('black')
    label.set_fontsize(10)

ax.tick_params(axis='y', colors='black', width=0.8)
for label in ax.get_yticklabels():
    label.set_color('black')
    label.set_fontweight('normal')
    label.set_fontsize(10)

if ylim:
    ax.set_ylim(ylim)

ax.yaxis.grid(True, color='gray', linestyle='--', linewidth=0.7, alpha=0.6)
sns.despine(left=False, bottom=False)

ax.set_title("Porosity Distribution", fontsize=14, fontweight='bold')

# Remove legend if present
if ax.get_legend() is not None:
    ax.get_legend().remove()

plt.tight_layout()
plt.show()
```

Code part

```
 #--- Loading ---
stack_path = r"C:\Users\LENOVO\Desktop\MON DOSSIER MEMOIR H2\image_stack_1.tiff"
stack = imread(stack_path)

def load_image(cur_num):
    img = stack[:, cur_num, :]
    return img

cur_num = 900
cur_img = load_image(cur_num)
print(cur_img.shape)
plt.imshow(cur_img, cmap='gray')
plt.axis('off')
plt.show()



 #--- image annotation ---
layer_definitions = {
    900: [((20, 260), (20, 1850)),
          ((290, 330), (20, 1850)),
          ((350, 420), (20, 1850)),
          ((440, 465), (20, 1850))]
}

#--- Model training---
# Extract the single slice image from your stack
y_index = 900
image = stack[:, y_index, :] #load_image(y_index)

# Create the mask for this slice
mask = create_mask(image, layer_definitions[y_index])

# Train the model with the single image and mask
trained_model = training_model(image, mask)



#--- Porosity and thickness calculation---
result_path= r"C:\Users\LENOVO\SOFC Data set\SAVE_IMAGE"
prefix = 'ttest_image_'
```

```
filename = prefix + "_results.csv"
fixed_thresholds = threshold_multiotsu(load_image(900), classes=5)
y_range = range(800,1001)

prefix='test_image_'
porosity, thickness = process_layer(
    trained_model, max_layer=3,
    fixed_thresholds=fixed_thresholds,
    idx_range=y_range,
    save_csv_path = os.path.join(result_path, filename)
)

#--- Plotting---

plot_porosity_comparison(
    [r"C:\Users\LENOVO\SOFC Data set\SAVE_IMAGE\test_image__results_porosity.csv"],
    "layer1 [%]", "layer2 [%]", "layer3 [%]",
    ylim=(0, 40)
)

plot_thickness_comparison(
    [r"C:\Users\LENOVO\SOFC Data set\SAVE_IMAGE\test_image__results_thickness.csv"],
     "layer2 [px]", "layer3 [px]",
    ylim=(0, 100)
)
```